Magnetosphere response to high-speed solar wind streams: A comparison of weak and strong driving and the importance of extended periods of fast solar wind

M. H. Denton[1,2] and J. E. Borovsky[3,4]

Received 30 August 2011; revised 11 January 2012; accepted 3 March 2012; published 1 May 2012.

[1] Much attention has been focused on the reaction of the magnetosphere to the solar wind during the recent extended solar minimum (2006–2010). Although this period was exceptionally quiet when categorized by some parameters (e.g., the number of sunspots) the solar wind still contained features which impacted the Earth's magnetosphere and caused geomagnetic disturbances. Recurrent corotating interaction regions (CIRs) and associated high-speed solar wind streams (HSSs) are typically associated with the declining phase of the solar cycle and were a regular feature of the solar wind during the most recent solar minimum. Here we compare and contrast strong and weak HSSs in the solar wind and their subsequent effect within the Earth's magnetosphere. We find significant differences between strong and weak HSS effects in the plasmasphere, in the ion and electron plasma sheets, and in the outer electron radiation belt. A density-temperature description of the outer radiation belt is shown to shed light on why the radiation belt flux is observed to return at a higher level after the arrival of strong HSSs than before strong HSSs and why the flux is observed to return at a lower level after the arrival of weak HSSs than before weak HSSs.

Citation: Denton, M. H., and J. E. Borovsky (2012), Magnetosphere response to high-speed solar wind streams: A comparison of weak and strong driving and the importance of extended periods of fast solar wind, *J. Geophys. Res.*, *117*, A00L05, doi:10.1029/2011JA017124.

1. Introduction

[2] The effect of high-speed solar wind streams (HSSs) on the ionosphere was likely observed even prior to the space age [e.g., *Bartels*, 1934]. Recurrent 27-day periodicities observed in the ionosphere (and subsequently in the magnetosphere) may be associated with coronal holes—the source of fast solar wind—close to the sun's equator. The recurrent nature of coronal holes, and the subsequent interaction of fast and slow solar wind, gives rise to corotating interaction regions (CIRs) and HSSs [e.g., *Tsurutani et al.*, 2006a, and references therein].

[3] Recently much attention has been focused on the reaction of the magnetosphere to the solar wind during the most recent extended solar minimum (2006–2010). Although this period was exceptionally quiet when categorized by some parameters (e.g., the number of sunspots) the solar wind still contained transient features which impacted the Earth's magnetosphere and caused geomagnetic disturbances. Recurrent CIRs and HSSs are typically associated with the declining phase of the solar cycle [e.g., *Tsurutani et al.* 1995; *Tsurutani et al.*, 2006a; *McPherron and Weygand*, 2006; *Liemohn and Chan*, 2007; *Kavanagh and Denton*, 2007; *Denton et al.*, 2008] and were a regular feature of the solar wind around the most recent solar minimum. Examination of the solar wind velocity, for example from measurements by the ACE satellite, indicates that as the most recent solar cycle progressed the HSSs tended to be of shorter duration with lower peak speeds than earlier in the cycle. Since HSSs are known to cause changes in the density and temperature of various plasma populations (e.g., ionosphere, plasma sheet, plasmasphere, radiation belt) it is important to investigate how the "strength" of HSSs (peak velocity and duration of fast wind) affects these changes.

[4] In this study we examine solar wind and geomagnetic plasma data and select a set of 22 "weak" HSSs which occurred between 2005 and 2007. The effect these events have on the electron and ion populations in various regions of the magnetosphere is studied and then compared with the effect of more robust "strong" HSSs that have been investigated previously using superposed epoch techniques. We also aim to determine whether a high-speed, solar-wind-stream-driven storm has a threshold effect, i.e., whether weaker driving results in weaker storm signatures or an absence of storm signatures. The terms *weak* and *strong* relate to the comparative duration and the fast solar wind and the peak velocity of the fast wind, and they are defined in detail below. Specifically, we investigate conditions in the

[1]Department of Physics, Lancaster University, Lancaster, UK.
[2]Also at Space Science Institute, Boulder, Colorado, USA.
[3]Los Alamos National Laboratory, Los Alamos, New Mexico, USA.
[4]AOSS Department, University of Michigan, Michigan, USA.

0148-0227/12/2011JA017124

solar wind, the plasmasphere, the ion and electron plasma sheets, and the outer electron radiation belt during weak HSSs and compare with the response of these populations during strong HSSs. By investigating various regions of geospace, and the changes which occur following onset of these repeatable events, we aim to document the strong-versus-weak system response of the magnetosphere during HSSs. Do all HSSs elicit the same response? Is the response linear? Are some parts of the system affected more than others during HSSs of different strength? Our results indicate that important differences in the magnetospheric response occur for weak HSSs compared to strong HSSs and that the duration of extended driving due to elevated solar wind velocity is an important cause of these differences. We show that a density-temperature description of the outer electron radiation belt has the potential to reveal new understanding of the phenomena of energetic electron flux dropouts during strong and weak HSSs. We conclude that when studying the dynamics of plasmas within the magnetosphere in response to HSSs it is crucial to consider the solar wind driver, its strength, and its time history, rather than to rely solely on internal magnetospheric indices.

2. Analysis: Event Selection and Data Sources

[5] Two sets of events are used in this study. The first set of "strong" events and subsets thereof (93 HSS events between 1993 and 2005) have previously been utilized to investigate thermal and energetic particle populations in the magnetosphere with respect to plasma evolution around geosynchronous orbit [*Denton and Borovsky*, 2008], plasmaspheric drainage plumes [*Borovsky and Denton*, 2008], the pre-storm decay of the radiation belts [*Borovsky and Denton*, 2009b], relativistic-electron flux dropouts and recoveries [*Borovsky and Denton*, 2009a], plasma-transport timescales [*Denton and Borovsky*, 2009], the heating of the outer electron radiation belt [*Borovsky and Denton*, 2010b], the magnetic field morphology of the magnetosphere [*Borovsky and Denton*, 2010a], and the anisotropy of the outer electron radiation belt [*Borovsky and Denton*, 2011b]. The 93 events used here were selected based on solar wind conditions recorded in the OMNI2 data set [*King and Papitashvili*, 2005]. The selection criteria for these "strong events" are defined as follows: (a) a clear west-to-east shear in the y-component of the solar wind velocity (which is indicative of the boundary between slow and fast wind), (b) the solar wind speed exhibits a sudden increase to speeds in excess of 550 km s^{-1}, (c) a local maximum in the solar wind density (indicative of the compression of slow solar wind by the following fast solar wind), and (d) an increase in the *Kp* index such that it exceeds 4 in the period immediately after the velocity shear. The precise zero epoch [*Ilie et al.*, 2010] for the events is the sudden onset of magnetospheric convection detected after the arrival of a HSS at the magnetopause as determined from the Midnight Boundary Index (MBI) [*Denton and Borovsky*, 2009]. The MBI is closely correlated with *Kp* and denotes the geographic latitude of the equatorward edge of precipitation [*Gussenhoven et al.*, 1983; *Elphic et al.*, 1999; *Thomsen*, 2004]. The duration of fast wind during these strong events is ~4–5 days.

[6] A new set of "weak" events occurring between 2005 and 2007 was constructed for comparison in this current study. This list of weak events comprises 22 HSSs selected based on solar wind conditions recorded in the OMNI2 data set [*King and Papitashvili*, 2005]. In brief these events were selected based on the following criteria; (a) a clear west-to-east shear in the y-component of the solar wind velocity (which is indicative of the boundary between slow and fast wind), (b) the solar wind speed exhibits a sudden increase to speeds in excess of 450 km s^{-1}, (c) a local maximum in the solar wind density (indicative of the compression of slow solar wind by the following fast solar wind), and (d) an increase in the *Kp* index such that it exceeds 3 in the period immediately after the velocity shear. Given the nature of the solar wind during the most recent declining phase and around solar minimum there were many equatorial coronal holes coexisting on the sun which led to repeated HSSs separated by only a few days as measured in the solar wind. There is thus no requirement for an extended calm period of days in the period prior to zero epoch. We note that the selection of these weak events is more difficult than the previous selection of strong events due to the reduced solar wind and magnetospheric HSS signature (resulting in a lower signal-to-noise ratio). A number of events were rejected due to uncertainty in whether the HSSs were accompanied by other transient solar wind conditions (e.g., the presence of ejecta). The duration of fast wind during these weak events is ~2 days.

[7] To reveal the solar wind conditions during these events four parameters from the OMNI2 database [*King and Papitashvili*, 2005] are studied. These are: (a) the magnitude of the solar wind velocity, (b) the y-component of the solar wind velocity, (c) the solar wind density, and (d) the product of the solar wind velocity and the negative z-component of the magnetic field, $-vB_z$ a proxy for the coupling between solar wind and magnetosphere. The subsequent geomagnetic conditions are revealed by study of the *Kp* index (a proxy for global magnetospheric convection), the MBI (a higher time resolution proxy for magnetospheric convection), the PCI (Polar Cap Index, a parameter closely correlated with the dayside reconnection rate) [*Troshichev et al.*, 1988], the *Dst* index (a proxy for the ring current or partial ring current strength [*Liemohn et al.*, 2001]), and the modified *Dst** index (the so-called pressure-corrected *Dst*—i.e., the *Dst* index with the effect of dayside magnetopause currents removed).

[8] To investigate how plasma parameters in the magnetosphere change before, during, and after HSS arrival at the magnetopause we study measurements of ions and electrons at geosynchronous orbit at various energies as outlined in the following three paragraphs:

[9] 1. For investigation of the plasmasphere and plasmaspheric drainage plume we utilize measurements of the cold (~1 eV) ion population made by the Magnetospheric Plasma Analyzer (MPA) flown on seven Los Alamos National Laboratory (LANL) satellites from geosynchronous orbit (GEO) in the period under study. A detailed description of this instrument is given by *Bame et al.* [1993], and the data analysis technique used to derive the cold ion density (as well as the hot ion and electron parameters) is described by *Thomsen et al.* [1999]. Previous studies of the cold ion behavior at GEO are contained in a number of studies [e.g., *Elphic et al.*, 1996; *Lawrence et al.*, 1999; *Su et al.*, 2001; *Denton et al.*, 2005]. Measurements of cold ion density, the percentage occurrence of high density cold plasma (>10 cm^{-3}), and the cold ion flow speed are utilized in

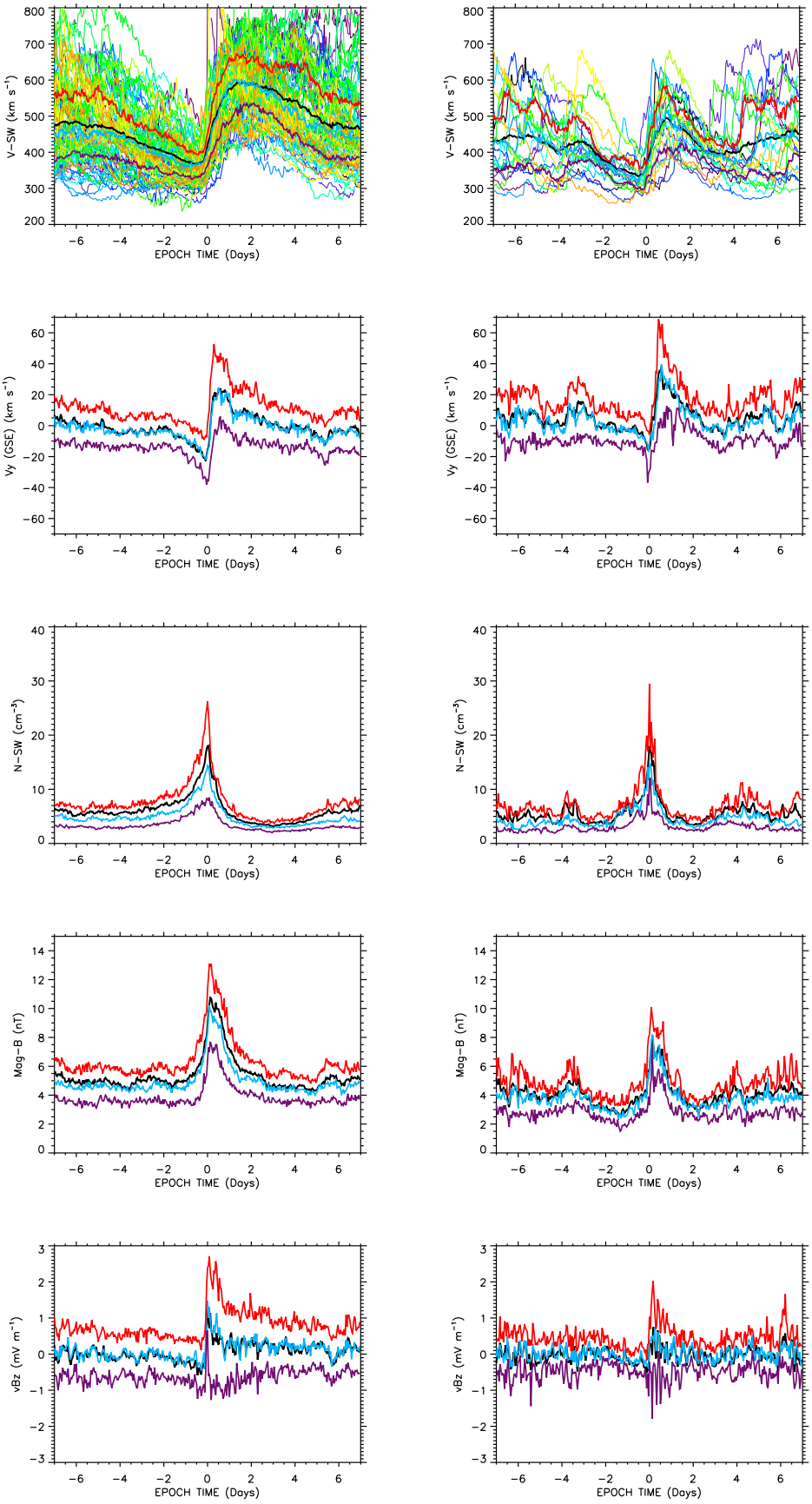

Figure 1

this study and we investigate how these parameters change as a function of epoch time.

[10] 2. For investigation of the plasma sheet population we utilize measurements of the hot (~0.03–45 keV) ions and electrons also made by the MPA instruments flown on seven LANL satellites in geosynchronous orbit [*Thomsen et al.*, 1999]. Previous studies of hot ion and electron behavior at GEO are contained in a number of studies [e.g., *McComas et al.*, 1993; *Borovsky et al.*, 1998a; *Korth et al.*, 1999; *Denton et al.*, 2005; *Lemon and O'Brien*, 2008; *MacDonald et al.*, 2008; *Thomsen et al.*, 2011]. Measurements of hot ion and electron density and hot ion and electron temperature are utilized in this study.

[11] 3. For investigation of the outer electron radiation belt we utilize measurements of the energetic electrons (~0.045–2.0 MeV) made by the Synchronous Orbit Particle Analyzer (SOPA) instruments onboard LANL satellites in geosynchronous orbit. A detailed description of this instrument is given by *Belian et al.* [1992] and *Cayton and Belian* [2007]. The methodology utilized to derive density and temperature from the data is described by *Cayton et al.* [1989; see also *Cayton and Belian*, 2007]. In brief SOPA detectors measure count rates of electrons in the energy range ~30 keV to >2 MeV every 10 s. The count rates (spin-averaged) are then used to determine differential measurements of flux. To generate density and temperature measurements the spin-averaged SOPA count rates are fitted with two relativistic Maxwellian components in addition to a flat "background" included to account for the quasi-constant flux of penetrating particles. The two Maxwellians pertain to a "soft" low-energy population (electrons with a distribution temperature ~30 keV) and a "hard" high-energy population (electrons with a distribution temperature ~150 keV) [*Cayton and Belian*, 2007; *Denton et al.*, 2010]. Relativistic bi-Maxwellian fits have previously been shown to be good fits to omnidirectional electron fluxes at geosynchronous orbit [*Cayton et al.*, 1989; *Pierrard and Lemaire*, 1996]. The lower-energy population is the suprathermal tail of the electron plasma sheet (typically associated with substorm injections) [*Lezniak et al.*, 1968; *Cayton et al.*, 1989; *Birn et al.*, 1998], while the harder spectra is the outer electron radiation belt [*Cayton et al.*, 1989; *Belian et al.*, 1996]. For every half-hour of data median values of the temperature and density fits are calculated and these medians are used in the current study. A density-temperature description of the radiation belts is fundamental in that the number density is a measure of the number of electron in the belt and the temperature is a measure of the spread of the particle distribution in velocity space. When the density goes up or down it indicates that electrons have arrived at or left the vicinity of the measuring spacecraft; when the temperature goes up or down it is an indication of heating or cooling (by selective loss), or that 'new' electrons with a different energy spectrum have arrived. The differential flux is linearly proportional to the number density but is a nonlinear, non-monotonic function of the temperature. When the flux goes up or down, it is very difficult to infer what is happening with the radiation-belt electron population. Along with the density-temperature description of the radiation belt, the more familiar flux picture is investigated utilizing pitch-angle-averaged and local-time-averaged fluxes from SOPA (described in detail by *Borovsky and Denton* [2009a]) and pitch-angle-resolved fluxes measured around midnight (described in detail by *Borovsky and Denton* [2011b]).

3. Results

3.1. Solar Wind

[12] Superposed solar wind quantities are plotted in Figure 1, which contains the superposed mean (thick black lines), median (thick light-blue lines), upper quartile (thick red lines), and lower quartile (thick purple lines) of various parameters for the 93 strong (left column) and 22 weak (right column) HSSs investigated in this study, from 5 days before to 5 days after zero epoch. The superposed average of the solar wind velocity (V_{SW}) is shown in the top row, with the y-component of the velocity (Vy) in the second row, the solar wind density (N_{SW}) in the third row, and product of solar wind velocity and inverse of the z-component of the magnetic field ($-vB_z$), a proxy for coupling between solar wind and magnetosphere, plotted in the fourth row. The top row also contains the individual traces of V_{SW} for each event (one color for each) to show the typical spread in values; these are omitted from the lower plots for clarity. Given that there are fewer events in the superposed analyses the statistics are somewhat less clear for the weak events compared to the strong events. However, meaningful conclusions can still be drawn.

[13] The average solar wind velocity (top row) slowly decreases to a local minima around zero epoch just prior to the rapid transition between fast and slow solar wind (characterized by the shear observed in the y-component of the solar wind velocity (second row). The density in the solar wind (third row), magnetic field magnitude (fourth row), and $-vB_z$ (bottom row) show the same average trends for the strong and weak events. The main differences between strong and weak events are: (1) the maximum solar wind velocity is higher for the strong events compared to the weak events (~600 km s^{-1} compared to ~500 km s^{-1}), and (2) the period of elevated fast solar wind persists for much longer for the strong events compared to the weak events; i.e., solar wind velocities exceed 500 km s^{-1} until ~5 days after zero epoch for the strong events, while in contrast for the weak events the solar wind speed falls below ~400 km s^{-1} after ~3 days. (Note: for the weak HSSs it is clear from examination of the solar wind that the wind speed starts to rise again after ~2–3 days after zero epoch, indicating the start of another HSS).

Figure 1. Superposed averages of solar wind parameters for 93 strong HSSs (left column) and 22 weak HSSs (right column) from five days before to five days after zero epoch). The plots show changes in the solar wind velocity (top row), *y*-component of the velocity (second row), solar wind density (third row), magnetic field magnitude (fourth row), and product of solar wind velocity and *z*-component of the magnetic field (bottom row). For each plot the thick black line denotes the mean, the thick light-blue line denotes the median, the thick red line denotes the upper quartile, and the thick purple line denotes the lower quartile, respectively. In the first row the individual traces of solar wind velocity are shown by the thin colored lines (one color per event).

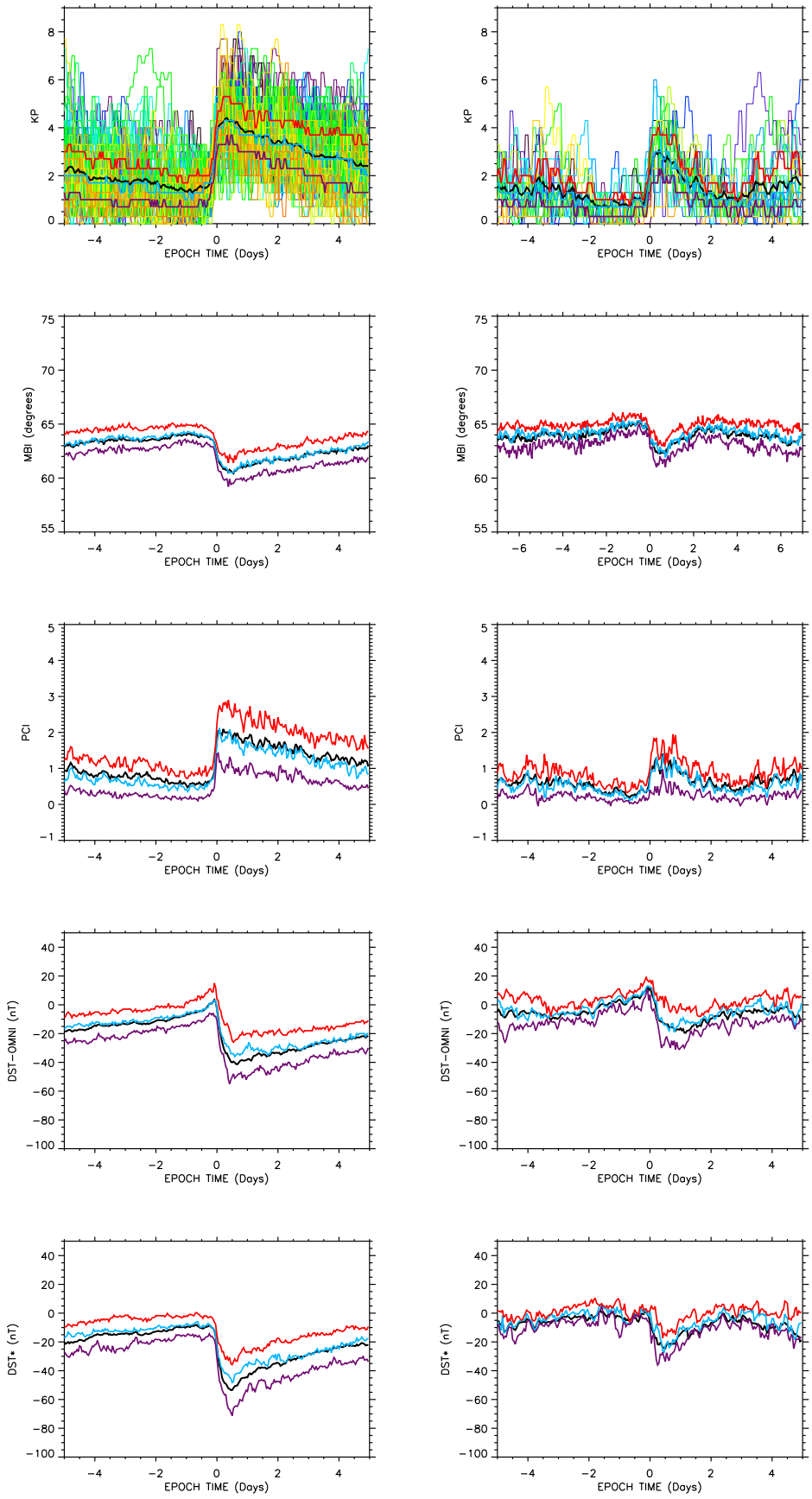

Figure 2

The extended duration of elevated solar wind velocity results in the coupling between solar wind and magnetosphere (proxied by $-vB_z$) being greater for the strong HSSs than for the weak HSSs.

3.2. Geomagnetic Activity

[14] Superposed geomagnetic activity parameters are plotted in Figure 2, which shows the superposed mean (thick black lines), median (thick light-blue lines), upper quartile (thick red lines), and lower quartile (thick purple lines) of various parameters for the 93 strong (left column) and 22 weak (right column) HSSs investigated in this study, from five days before to five days after zero epoch. The superposed average of the *Kp* index is shown on the top row, with the MBI in the second row, the PCI in the third row, the *Dst* index in the fourth row, and the derived *Dst** index in the bottom row. The top row also contains the individual traces of *Kp* for each event (one color for each) to show the typical spread in values; these are omitted from the lower plots for clarity.

[15] The trends of in all five parameters shown in Figure 2 are similar for the strong and weak events. For both the strong and weak HSS events enhanced geomagnetic activity (parameterized by *Kp*, MBI, PCI, *Dst*, and *Dst**) commences sharply at zero epoch and then declines smoothly to pre-event levels. Magnetospheric convection (proxied by *Kp* and MBI) remains elevated for days following zero epoch, as does the rate of dayside reconnection (proxied by PCI). Two clear differences between strong and weak events are apparent: (1) average geomagnetic activity (*Kp* index) in the period prior to zero epoch falls to a lower level for the weak events compared to the strong events, and (2) the elevated activity after the zero epoch is sustained for longer for the strong HSS events (~5 days) than for the weak HSS events (~2 days). These tally closely with the durations of elevated solar wind velocity shown in Figure 1 (top row). The extended period of fast wind (coupled with southward IMF) drives the elevated levels of geomagnetic activity. Note: the strength of the ring current (proxied by the *Dst* and *Dst** indices) shows only a weak response to HSS arrival (typical maximum average reduction in *Dst* is ~20–40 nT consistent with only very minor storm activity): the magnetosphere driven by HSSs does not contain a highly effective ring current or partial ring current.

3.3. Plasmasphere

[16] Figure 3 contains plots of parameters pertaining to plasmasphere behavior during HSSs plotted as a function of epoch time (*x* axis: 1 h time resolution) and local time around geosynchronous orbit (*y* axis: 1 h time resolution) from 5 days before to 5 days after zero epoch. Each plot contains the average of more than 60, 000 independent data points (weak events) with plots for the 93 strong HSSs shown in the left column and plots for 22 weak HSSs shown in the right column. The superposed average of the cold ion density (~1 eV) is shown in the top row, with the percentage occurrence that the cold ion density exceeds 10 cm^{-3} shown in the middle row, and the cold ion equatorial-plane flow speed shown in the bottom row. The percentage occurrence of high density cold plasma (middle row) following zero epoch highlights the presence of plasmaspheric plume material typically detected at GEO in the afternoon sector [e.g., *Chappell*, 1974; *Chen and Grebowsky*, 1974; *Spiro et al.*, 1981; *Elphic et al.*, 1996; *Borovsky and Denton*, 2006a].

[17] It is clear that there significant differences between the strong and weak HSS events, despite the similarities in the geomagnetic indices for each type of event at zero epoch. In general the density of cold plasmaspheric ions (top row) increases prior to zero epoch. This occurs during the reduced geomagnetic activity (the "calm before the storm") prior to HSS arrival at the magnetopause [*Borovsky and Steinberg*, 2006; *Borovsky and Denton*, 2009b]. The outer plasmasphere fills during intervals of low geomagnetic activity and may grow to extend to beyond geosynchronous orbit [*Sojka and Wrenn*, 1985; *Su et al.*, 2001], particularly in the afternoon/dusk sector [*Chappell et al.*, 1970; *Carpenter et al.*, 1993]. The plasmasphere density prior to HSS onset is much higher for the weak events than for the strong events. This is expected since the level of geomagnetic activity prior to HSS onset is lower for the weak events than for the strong events (see Figure 2). Subsequently the detection of high density cold plasma (middle row) following zero epoch is much greater for the weak events than for the strong events. This is consistent with plasmasphere material (from a comparatively denser plasmasphere during the weak HSSs) being convected to the dayside in a plasmaspheric plume [*Borovsky and Denton*, 2006a; *Denton and Borovsky*, 2008; *Borovsky and Denton*, 2008]. The cold ion flow speed in the equatorial plane (bottom row) also fits this picture. For both weak and strong events the cold ions are corotating prior to HSS arrival with the speed maximized around dawn and dusk. Following the onset of geomagnetic activity (and convection) the plasmaspheric material moves to the dayside with an average convection speed of ~12–16 km s^{-1} for the strong HSS events and an average convection speed of ~8–12 km s^{-1} for the weak HSS events [cf. *Denton et al.*, 2007; *Denton and Borovsky*, 2008; *Borovsky and Denton*, 2008].

3.4. Plasma Sheet

[18] Figure 4 contains plots of parameters pertaining to the plasma sheet behavior during HSSs plotted as a function of epoch time (*x* axis: 1 h time resolution) and local time around geosynchronous orbit (*y* axis: 1 h time resolution) from 5 days before to 5 days after zero epoch. Each plot contains the average of more than 60, 000 independent data points (weak events) with plots for the 93 strong HSSs shown in the left column and plots for 22 weak HSSs shown

Figure 2. Superposed averages of magnetospheric indices for 93 strong HSSs (left column) and 22 weak HSSs (right column) from five days before to five days after zero epoch). The plots show changes in the *Kp* index (top row), the MBI (second row), the PCI (third row), the *Dst* index (fourth row), and the derived *Dst**, pressure-corrected, index). For each plot the thick black line denotes the mean, the thick light-blue line denotes the median, the thick red line denotes the upper quartile, and the thick purple line denotes the lower quartile, respectively. In the first row the individual traces of *Kp* are shown by the thin colored lines (one color per event).

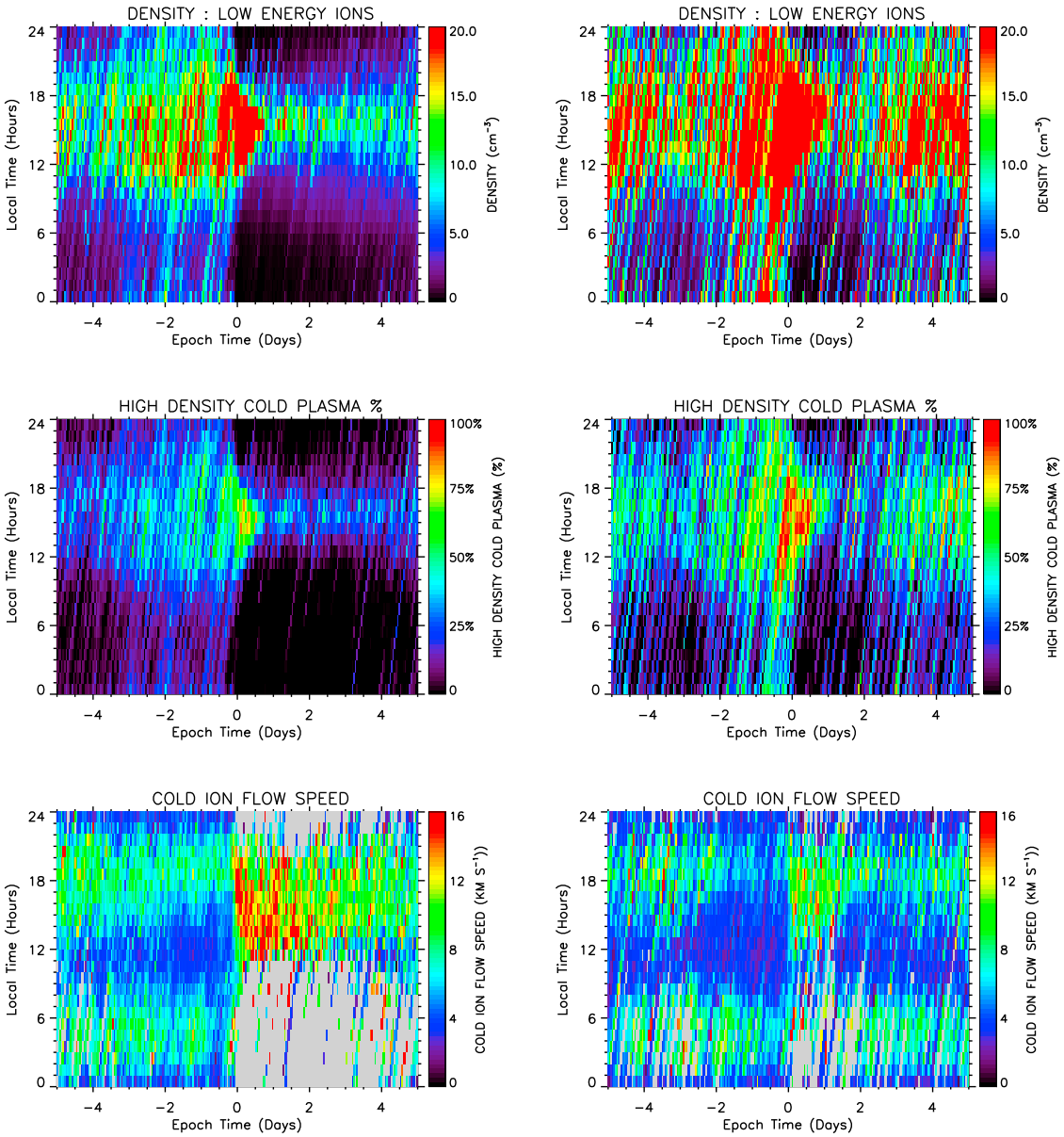

Figure 3. Superposed averages of plasmaspheric parameters measured at geosynchronous orbit for 93 strong HSSs (left column) and 22 weak HSSs (right column) from five days before to five days after zero epoch). The plots show changes in the cold ion density (top row), occurrence frequency of high density (>10 cm^{-3}) cold plasma (second row), and cold ion flow speed (bottom row). Prior to zero epoch the plasma is corotating with the Earth and the plasma measured is assumed to be part of the plasmasphere. Immediately following zero epoch the plasma moves toward the dayside magnetopause and is assumed to form part of a plasmaspheric drainage plume.

in the right column. The superposed average of the hot ion density (~0.03–40 keV) is shown on the top row, with the hot ion temperature shown on the second row, the hot electron density (~0.1–40 keV) shown on the third row, and hot electron temperature shown on the bottom row.

[19] The plasma sheet parameters shown in Figure 4 demonstrate similar average trends for both the strong and weak HSS events. At zero epoch the onset of convection is accompanied by a sharp increase in the average hot ion density (top row) and the average hot electron density (third row) on the nightside and in the dawn/dusk sectors, which lasts <1 day (and is briefer for the weak events). This is consistent with the entry of high-density solar wind (third panel of Figure 2) into the magnetosphere to produce a superdense plasma sheet [*Borovsky et al.*, 1998a; *Denton and Borovsky*, 2009]. The ion temperature (second row) and the electron temperature (bottom row) show sudden increases at zero epoch, and these persist for a number of days. For the ions (second row) the temperature is elevated for ~3 days for the strong events and ~2 days for the weak events. For the electrons (bottom row) the temperature is elevated for ~5 days for the strong events and ~1.5 days for

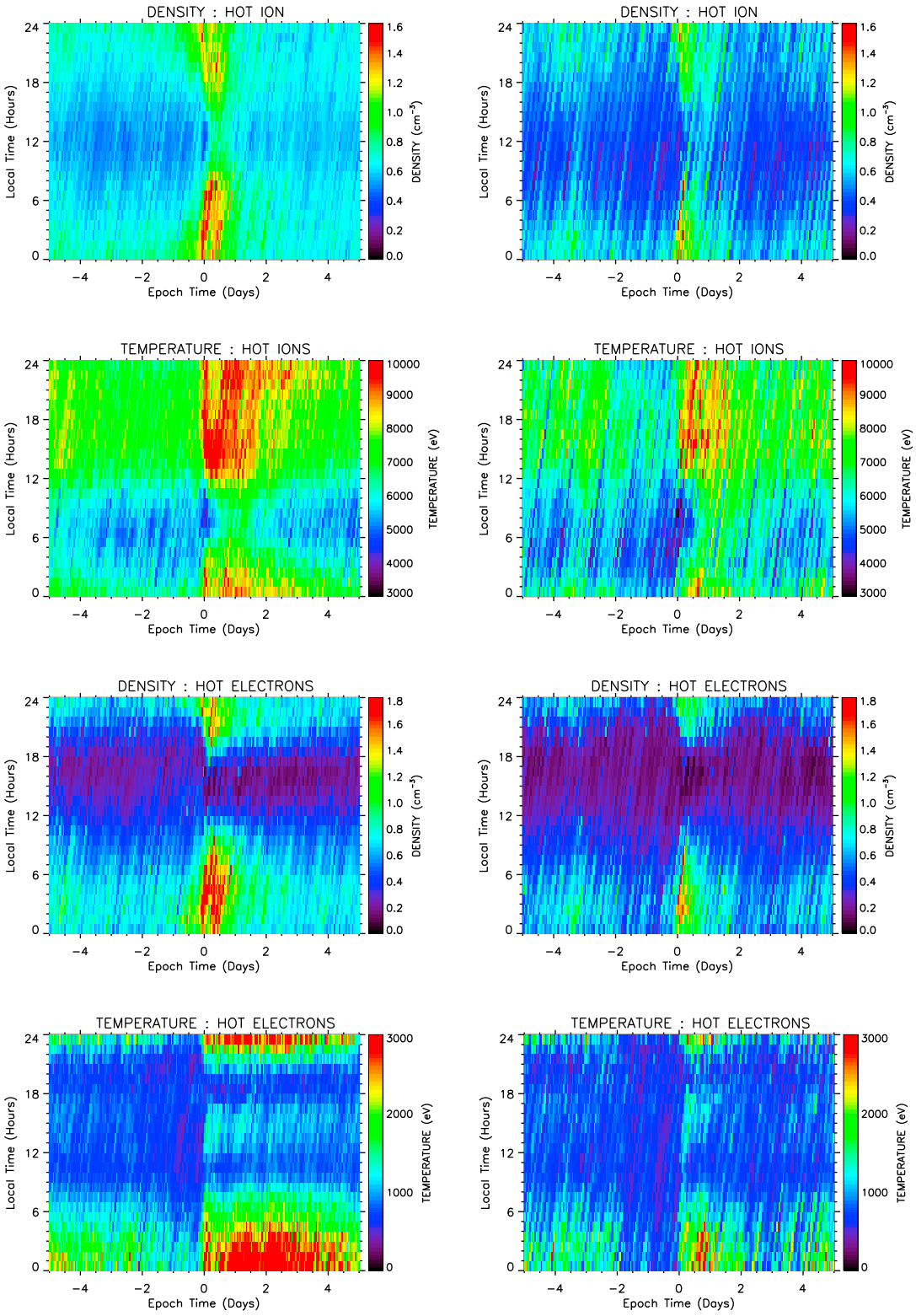

Figure 4. Superposed averages of plasma sheet parameters measured at geosynchronous orbit for 93 strong HSSs (left column) and 22 weak HSSs (right column) from five days before to five days after zero epoch). The plots show changes in the hot ion density (top row), hot ion temperature (second row), hot electron density (third row), and hot electron temperature (bottom row). Prior to zero epoch the electron and ion plasma density falls to low values (and the plasma sheet itself is assumed to be tailward of geosynchronous orbit on the nightside. Immediately following zero epoch the electron and ion density and temperature increase sharply and the plasma measured is assumed to be freshly injected plasma sheet material.

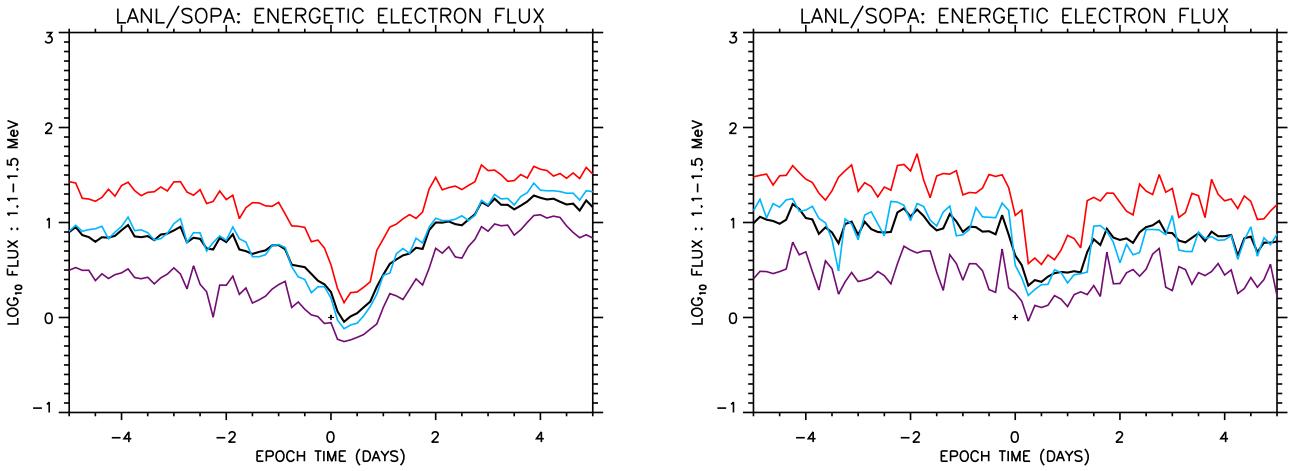

Figure 5. Superposed multisatellite averages of electron flux (1.1–1.5 MeV) measured at geosynchronous orbit for 93 strong HSSs (left) and 22 weak HSSs (right) from five days before to five days after zero epoch). For each plot the thick black line denotes the mean, the thick light-blue line denotes the median, the thick red line denotes the upper quartile, and the thick purple line denotes the lower quartile, respectively. For the strong HSSs the flux falls close to zero epoch and returns to a higher average flux level. For the weak HSSs the flux falls close to zero epoch and returns to a lower average flux level.

the weak events. It should be emphasized that the calculations of 'bulk' plasma sheet temperature and density discussed here cover the energy range ~0.03–45 keV. This energy interval spans the range of plasma sheet energies including the high energy tail, the suprathermal population. This is discussed separately in section 3.5. A detailed description and discussion of the "extra-hot" plasma sheet driven by fast solar wind previously observed for the strong HSS events may be found in *Denton and Borovsky* [2009]. (Note: the superhot, superdense plasma sheet is distinct from the cold dense plasma sheet which is correlated with extended periods of northward IMF [*Thomsen et al.*, 2003; *Lavraud et al.*, 2005, 2006] and may also be detected at GEO following the onset of geomagnetic activity). The plasma sheet electron temperature at GEO is known to correlate very well with solar wind velocity [*Borovsky et al.*, 1998a], and this has important implications for satellite operations and subsequent instrument longevity (see Appendix A).

3.5. Outer Electron Radiation Belt and Suprathermal Plasma Sheet

[20] Figure 5 contains plots of the multisatellite, local-time-averaged energetic electron flux measured at geosynchronous orbit as a function of epoch time from five days before to five days after zero epoch (3-h bins in epoch time are used in the averaging). The plots contain the superposed mean (thick black lines), median (thick light-blue lines), upper quartile (thick red lines), and lower quartile (thick purple lines) of the flux for 93 strong (left column) and 22 weak (right column) HSSs investigated in this study).

[21] For the strong HSS events (left plot) the average flux exhibits a slow decline prior to zero epoch, a rapid decrease close to zero epoch and reaches a minimum (the flux "dropout") within a few hours of the HSS arrival at the magnetopause. Over the following days the flux recovers and reaches a level in excess of its average pre-storm value. The reduction in flux prior to storm onset, and the dropout behavior itself, have previously been explained in terms of losses due to the growth of the plasmasphere during the calm before the storm [*Borovsky and Steinberg*, 2006; *Borovsky and Denton*, 2009b], combined with a sudden reduction in flux at storm onset [*Freeman*, 1964; *Nagai*, 1988; *Onsager et al.*, 2002; *Morley et al.*, 2010]. For the weak HSS events (right plot) the flux exhibits a similar dropout following HSS arrival at the magnetopause and a similar recovery. There is little evidence of a reduction in flux prior to zero epoch (even though these events exhibit very calm geomagnetic conditions prior to zero epoch) and upon recovery the average flux does not achieve its pre-storm level. The average flux has previously been reported to recover to levels below, equal to, or in excess of its pre-storm value [*Reeves et al.*, 2003]. We draw no conclusions as to the causes of the dropout itself (whether losses are due to scattering, transport, or magnetopause shadowing).

[22] The local time dependence of energetic electrons at GEO is strong due to so-called drift shell splitting [*Hones*, 1963; *Pfitzer et al.*, 1969; *Selesnick and Blake*, 2002], wherein electrons of different pitch angles follow different drift paths as they orbit the Earth. To investigate the pitch angle behavior of energetic electrons at geosynchronous orbit during HSSs we examine pitch angle resolved fluxes close to local midnight only. Figure 6 contains plots which reveal the pitch angle and energy-dependent behavior of the energetic electron flux in the region close to local midnight (22:00–02:00 LT). The left column pertains to the 93 strong HSSs and the right column pertains to the 22 weak HSSs. The plots show the mean value of the parameter in question from five days before to five days after zero epoch. The plots on the first and second rows pertain to the energetic electron flux as a function of epoch time (x axis: 1 h bins) and energy (y axis: 10 energy bins between ~0.04 and 1.7 MeV) for specific pitch angle range-normalized fluxes (flux/mean flux) are shown (where the mean flux is the average flux

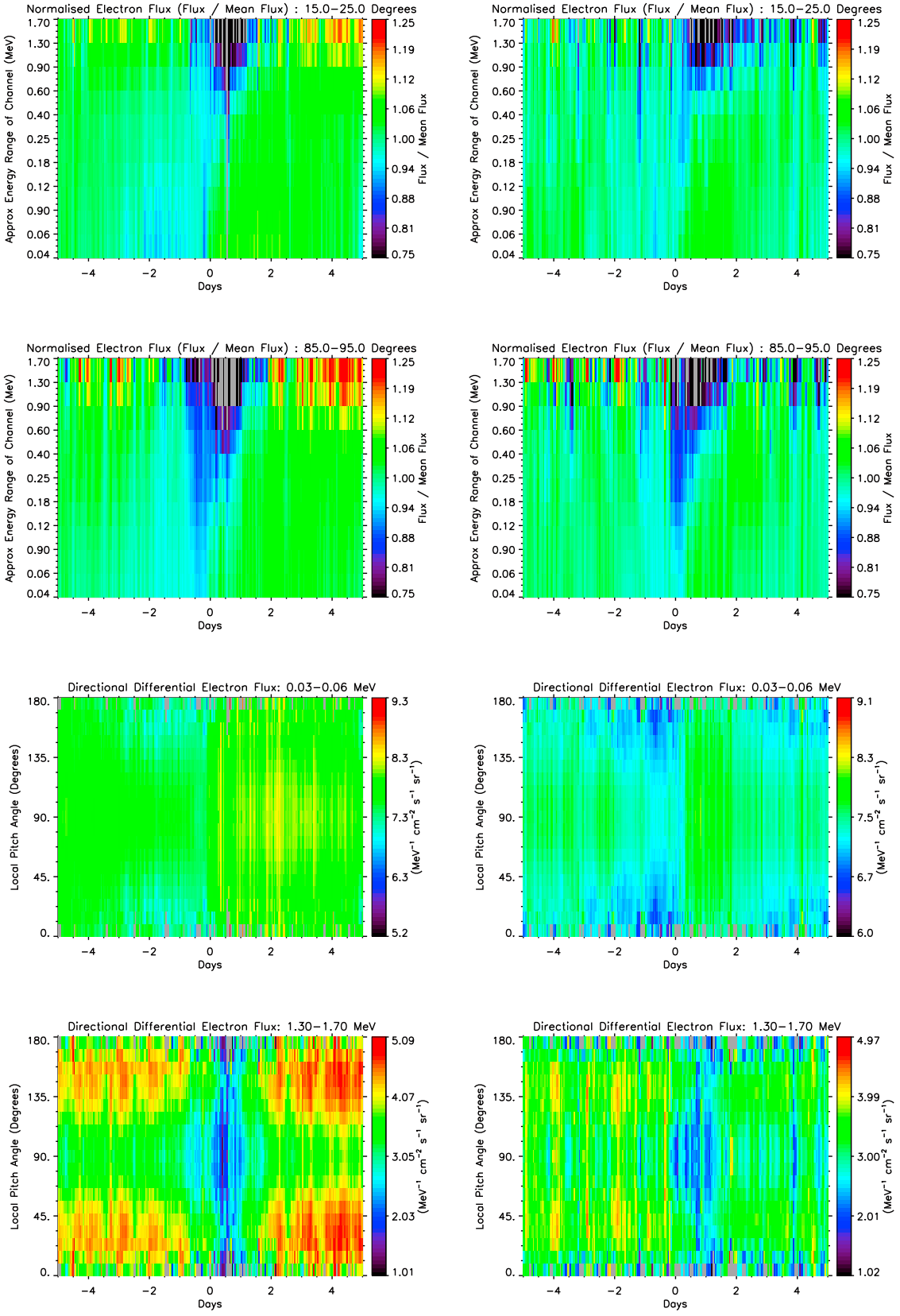
Normalised Electron Flux (Flux / Mean Flux) : 15.0–25.0 Degrees
Approx Energy Range of Channel (MeV)
Flux / Mean Flux
Days
Normalised Electron Flux (Flux / Mean Flux) : 85.0–95.0 Degrees
Directional Differential Electron Flux: 0.03–0.06 MeV
Local Pitch Angle (Degrees)
(MeV⁻¹ cm⁻² s⁻¹ sr⁻¹)
Directional Differential Electron Flux: 1.30–1.70 MeV

Figure 6

value at a particular energy for ±35 days around the zero epoch). The top row shows the normalized flux for pitch angles between 15 and 25° (∼parallel) and the second row shows the normalized flux for pitch angles between 85 and 95° (∼perpendicular). The plots on the third and fourth rows pertain to the energetic electron flux as a function of epoch time (*x* axis: 1 h bins) and pitch angle (*y* axis: 18 pitch angle bins) for a specific energy range. The third row shows the flux for energies between ∼30 and 60 keV (suprathermal plasma sheet) and the fourth row shows the flux for energies between ∼1.3 and 1.7 MeV (outer electron radiation belt).

[23] The results plotted in Figure 6 reveal important differences between flux behavior during strong HSSs compared to flux behavior during weak HSSs. For the strong HSS events the quasi-parallel fluxes (left column, top row) slowly decrease prior to zero epoch with the lower energies (∼60 keV) slowly falling for up to ∼2 days before HSS arrival. This corresponds to the period when geomagnetic activity becomes very weak and hence the lower energy electrons (with ∼suprathermal plasma sheet energies) follow drift paths that may not cross geosynchronous orbit [*Korth et al.*, 1999]. Close to zero epoch the higher energy fluxes (>1 MeV) fall rapidly (the dropout) and remain at low values for ∼1.5 days. As the recovery from dropout proceeds, the higher energy electron fluxes are elevated in excess of their pre-storm values. The overall picture is one in which the low energy fluxes return very quickly (∼hours) following HSS arrival while the higher energy electrons recovery over a more extended period (∼days). For the weak HSS events the quasi-parallel electron fluxes (right column, top row) exhibit behavior similar to that of the strong HSS events prior to dropout. However, in the period following zero epoch the fluxes at high energies (>1 MeV) take longer to recover, and the flux level does not exceed the pre-storm value. The behavior of the quasi-perpendicular electron fluxes (second row) is similar to that of the quasi-parallel fluxes; however, for both the strong HSS (left column) events and the weak HSS (right column) events, the reduction in flux for quasi-perpendicular electrons is comparatively greater than for quasi-parallel electrons at storm onset, as is the increase in flux during the recovery from dropout. We draw no conclusions as to the causes of the dropout (whether losses due to scattering, transport, or magnetopause shadowing).

[24] The pitch angle distributions of the electrons in the suprathermal plasma sheet (∼60 keV) at midnight are shown in the third row of Figure 6 for strong HSS events (left column) and weak HSS events (right column). The midnight suprathermal electron distribution for the strong HSSs is typically quasi-isotropic throughout with the flux falling slowly prior to zero epoch and recovering to values in excess of the pre-storm flux level at storm onset. For the weak HSS the suprathermal electron distribution is initially quasi-isotropic ∼4 days prior to zero epoch and becomes increasingly perpendicular close to zero epoch, consistent with losses due to scattering and other processes which occur preferentially for electrons with parallel pitch angles. Around zero epoch the distribution becomes quasi-isotropic once more, consistent with the injection of fresh plasma sheet electrons [cf. *Denton et al.*, 2005].

[25] The pitch angle distributions of the highly energetic electrons (>1 MeV) at midnight are shown in the bottom row of Figure 6 and are strongly anisotropic prior to HSS arrival, with both strong HSS events (left column) and weak HSS events (right column) exhibiting so-called "butterfly" distributions [*Fritz et al.*, 2003] dominated by parallel fluxes. The fluxes of the electrons for strong HSS events at all pitch angles reduce rapidly close to zero epoch and recover ∼1 day following zero epoch with flux levels exceeding their pre-storm value. During the weak HSS events the flux levels also dropout close to zero epoch and recover after ∼1 day, but the flux never achieves its pre-storm value.

[26] Although the behavior of the outer electron radiation belt is typically described in terms of the fluxes measured over a particular energy range, as discussed immediately above, it is also important to realize that the flux measured at a spacecraft is dependant on the underlying physical quantities, the density and the temperature, of the electron distribution. These quantities have previously been shown to potentially reveal a clearer picture of the physics of the outer electron radiation belt and energetic particles in the magnetotail operating during HSSs and during other dynamic geophysical conditions [*Borovsky et al.*, 1998b; *Borovsky and Cayton*, 2011; *Denton et al.*, 2010; *Denton and Cayton*, 2011; *Borovsky and Denton*, 2011a]. Section 2 contains details of how the SOPA measurements of flux can be fitted with relativistic bi-Maxwellians to give density and temperature values for co-located "soft" and "hard" populations of electrons. The soft low-energy population is the suprathermal plasma sheet (temperature of distribution ∼30 keV) and the hard population is the outer electron radiation belt (temperature of distribution ∼150 keV). Figure 7 contains plots showing the behavior of these plasmas calculated using the methodology described in section 2 and also in *Cayton et al.* [1989] and *Cayton and Belian* [2007]. The plot contains the superposed average parameter as a function of epoch time (*x* axis: 1 h bins) and local time (*y* axis: 1 h bins) with the left column pertaining to the 93 strong HSSs and the right column pertaining to the 22 weak HSSs. The plots contain the mean value of each parameter from five days before to five days after zero epoch. The top row shows the superposed mean energetic electron density, the second row shows the superposed mean energetic electron

Figure 6. Superposed averages of electron radiation belt parameters measured at geosynchronous orbit close to local midnight for 93 strong HSSs (left column) and 22 weak HSSs (right column) from five days before to five days after zero epoch). The plots show changes in normalized quasi-parallel electron flux as a function of energy (top row), normalized quasi-perpendicular electron flux as a function of energy (second row), electron flux as a function of pitch angle for energies ∼30–60 keV (third row), and electron flux as a function of pitch angle for energies ∼1.3–1.7 MeV (bottom row). The lower energy electrons display a quasi-isotropic flux distribution and display a flux increase close to zero epoch (fresh injection of plasma sheet material). The higher energy electrons display a quasi-parallel distribution before and after zero epoch, with fluxes recovering over the following few days.

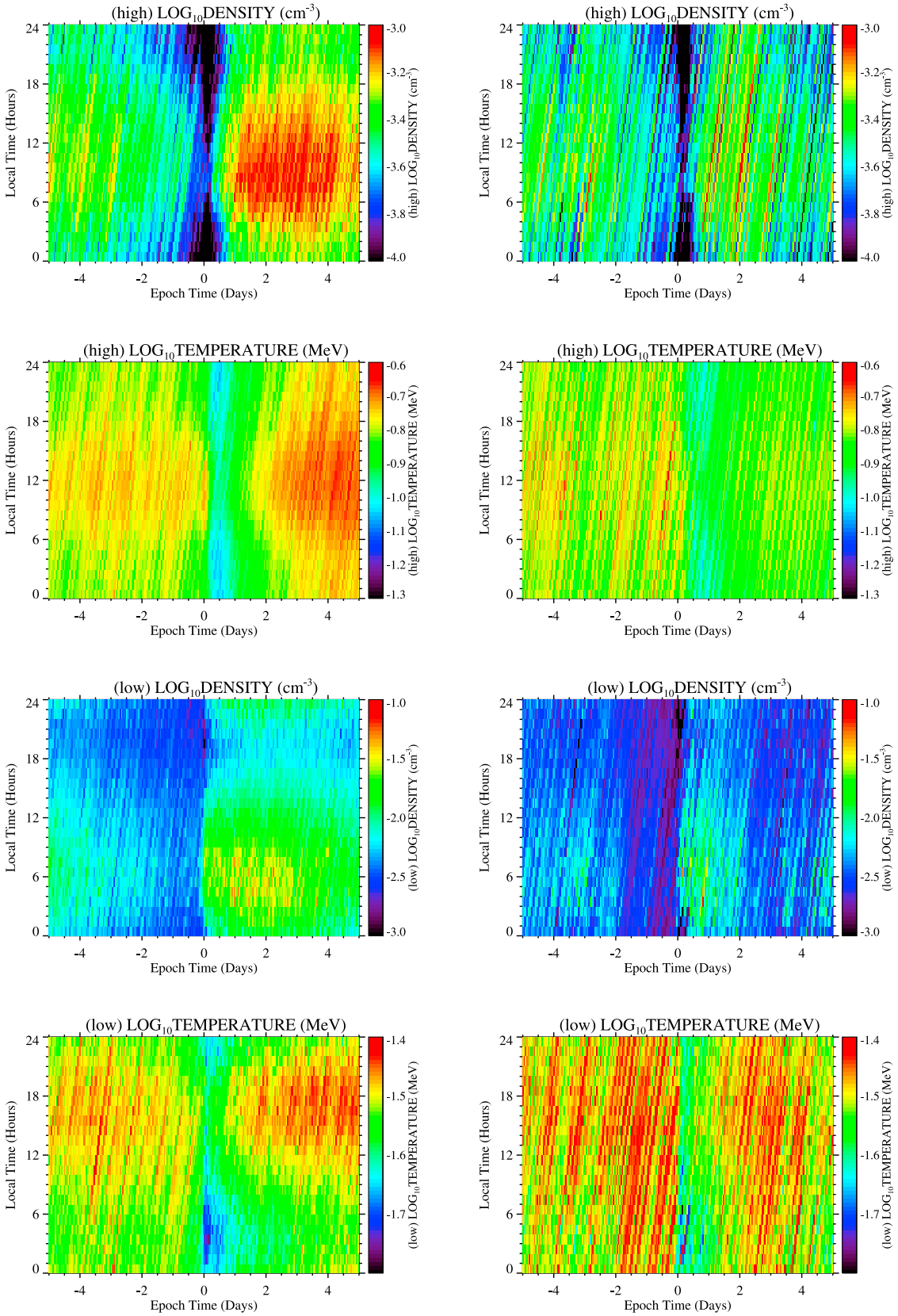
(high) LOG10DENSITY (cm-3)
(high) LOG10DENSITY (cm-3)
(high) LOG10TEMPERATURE (MeV)
(high) LOG10TEMPERATURE (MeV)
(low) LOG10DENSITY (cm-3)
(low) LOG10DENSITY (cm-3)
(low) LOG10TEMPERATURE (MeV)
(low) LOG10TEMPERATURE (MeV)
Local Time (Hours)
Epoch Time (Days)

Figure 7

temperature, the third row shows the superposed mean suprathermal electron density and the bottom row shows the superposed mean suprathermal electron temperature.

[27] The average outer electron radiation belt density (Figure 7, top row) exhibits a clear series of changes prior to, during, and after the arrival of HSSs for both strong HSSs (left plot) and weak HSSs (right plot). For the strong HSSs the density falls slowly prior to zero epoch and then undergoes a sudden dropout a few hours before HSS onset. This occurs as a result of the compressed slow solar wind impacting on the magnetosphere [*Gosling et al.*, 1978; *Borovsky and Denton*, 2009a] The dropout lasts a few hours and then recovery occurs with the density increasing to values much higher than those before the storm. The picture is similar for the weak HSSs and (in contrast with the fluxes summarized in Figures 5 and 6) the density again exceeds its pre-storm value. The temperature of the outer electron radiation belt distribution (second row) indicates that for strong HSSs (left plot) the electron distribution is at a roughly constant temperature prior to zero epoch, falls rapidly around zero epoch, and then recovers and increases over the next few days to a level in excess of its pre-storm value. For weak HSSs (right plot) the temperature is roughly constant prior to zero epoch, falls sharply around zero epoch, and then recovers slowly over the next few days. In contrast to the strong HSSs, the temperature remains much lower than its pre-storm level. The obvious conclusion to draw from the density and temperature behavior is that the density recovers and indeed exceeds its pre-event level. Following dropout a population of electrons returns to GEO during both weak and strong HSSs. However, this population is at a lower temperature during weak HSSs than during strong HSS. In addition the heating of the electrons over the subsequent days appears greater during the strong HSSs than during the weak HSSs. We draw no conclusions as to the causes of the dropout itself.

[28] Figure 7 also contains plots of the averaged suprathermal plasma sheet density (third row) and temperature (bottom row) for strong HSSs (left column) and weak HSSs (right column). These plots demonstrate behavior that is different to that found in the bulk plasma sheet (Figure 4) and summarized in section 3.4. It should be noted that the suprathermal population has very different access to geosynchronous orbit than the bulk plasma sheet population and hence we may expect different behavior when we compare the suprathermal density and temperature (Figure 7) to that for the bulk plasma sheet (Figure 4). The suprathermal electron density at GEO slowly falls prior to zero epoch and then increases sharply at HSS arrival for both strong and weak events. The density remains above pre-storm levels during the strong events for at least four days as elevated levels of magnetospheric convection are sustained (see Figure 2). For the weak events the suprathermal electron density remains elevated above pre-storm levels for a couple of days but then falls again once magnetospheric convection is reduced (see Figure 2). The temperature of the suprathermal electron plasma sheet (bottom row) is roughly constant prior to zero epoch for both weak and strong HSSs falling to a minimum close to HSS arrival. The electron temperature returns to, or exceeds, the pre-storm level for both weak and strong HSSs roughly one day after zero epoch.

4. Discussion

[29] The overall picture to be drawn from the above analyses, and from the results shown in Figures 1–7, is of a magnetospheric system during HSSs which is driven, and responds, primarily to changes in the solar wind. Detailed descriptions of the timing of changes in the magnetosphere in response to the arrival of HSSs at the magnetopause have been given in earlier studies [see *Borovsky and Denton*, 2009a, Table 1], along with the estimated transport times of plasma from the solar wind to the inner magnetosphere [*Denton and Borovsky*, 2009]. Below we list the observations outlined in section 3 and discuss their implications for the dynamics of the magnetosphere system as a whole.

[30] The main difference between the weak HSSs and the strong HSSs studied in this report is the peak level of solar wind velocity and the duration that fast solar wind bathes the magnetosphere. The average peak velocity for the strong HSSs is $\sim$600 km s^{-1} compared to $\sim$500 km s^{-1} for weak HSSs (see Figure 1). The duration of the fast solar wind is $\sim$4–5 days for the strong HSSs compared with $\sim$2 days for the weak HSSs (see Figure 1). Other averaged solar wind parameters (e.g., density, magnetic field magnitude) are very similar between the two types of events. This leads us to conclude (as others have done previously) that the solar wind velocity, in combination with the southward component of the IMF ($-vB_z$) are the variables which largely govern the magnetospheric response to HSSs.

[31] Investigation of the geomagnetic indices during weak and strong HSSs indicates that the level of magnetospheric convection (proxied by *Kp* and MBI) is elevated for the same duration as that of elevated solar wind speed. The dayside reconnection rate (proxied by PCI) is also elevated while the solar wind speed remains high. In contrast, while the ring current and partial ring current (proxied by *Dst* and *Dst** indices) do respond to weak and strong HSSs, the perturbation in *Dst* is weak indicating a weak ring current.

[32] With regard to the dynamics of the inner magnetosphere the period of calm that precedes HSSs is of great importance. The density in the plasmasphere is greater during extended periods of calm (weak HSS events) and hence the plasmaspheric plume density following convection onset

Figure 7. Superposed averages of density and temperature for electrons in the radiation belt and electrons in the suprathermal plasma sheet measured at geosynchronous orbit for 93 strong HSSs (left column) and 22 weak HSSs (right column) from five days before to five days after zero epoch). The plots show changes in the radiation belt electron density (top row), radiation belt electron temperature (second row), suprathermal electron density (third row), and suprathermal electron temperature (bottom row). The radiation belt electron density displays a dropout and sudden recovery to greater than its pre-dropout level for both strong and weak HSSs. The radiation belt electron temperature is higher than its pre-dropout value for the strong HSSs and lower than its pre-dropout value for the weak HSSs. The lower energy electrons display a density increase close to zero epoch (fresh injection of plasma sheet material).

is greater for weak HSS events than for strong HSS events However, the plumes are of shorter duration for the weak HSSs and persist only while magnetospheric convection is elevated. If pitch angle scattering by EMIC waves inside plasmaspheric plumes is an important loss process for radiation belt electrons [e.g., *Kovalevskiy*, 1980, 1981; *Jordanova et al.*, 2006; *Thorne et al.*, 2006; *Summers et al.*, 2007; *Rodger et al.*, 2008; *Borovsky and Denton*, 2009a; *Fraser et al.*, 2010], then clearly the strength of HSS is important for radiation belt losses also. Similarly, if pitch angle scattering by plasmaspheric hiss [e.g., *Lyons et al.*, 1972; *Meredith et al.*, 2006; *Lam et al.*, 2007; *Borovsky and Denton*, 2009b] occurs during the calm prior to HSS onset, then the higher density levels in the plasmasphere prior to weak HSSs should cause a different level of scattering in comparison to that found during strong HSSs where the plasmasphere is less dense prior to HSS arrival.

[33] The plasma sheet exhibits similar behavior during strong HSSs as during weak HSSs with the main difference being (1) the duration of superdense plasma sheet that occurs early in the storm, and (2) the duration of elevated temperatures in the ion and electron plasma sheets associated with the duration of the fast wind. Both (1) and (2) are longer for strong HSS events than for weak HSS events. In the case of the plasma sheet, weak driving gives a weak response. Specifically the average temperature of the plasma sheet (particularly the electron plasma sheet) remains elevated while ever fast solar wind bathes the magnetosphere [see also *Borovsky et al.*, 1998a; *Denton and Borovsky*, 2009]. This is of the order of 1–2 days for weak HSSs and ~5 days for the strong HSSs examined in this study. Plasma sheet temperature is an important parameter for plasma diamagnetism [*Borovsky et al.*, 1998b; *Borovsky and Denton*, 2010a], for ring current injections [*Ebihara and Ejiri*, 2000; *Liemohn et al.*, 2001; *Kozyra and Liemohn*, 2003; *Lavraud et al.*, 2005, 2006], and for spacecraft charging [*DeForest*, 1972; *Hastings and Garrett*, 1996; *Borovsky et al.*, 1998b; *Denton et al.*, 2006].

[34] The outer electron radiation belt is known respond to solar wind velocity [*Paulikas and Blake*, 1979; *Fung and Tan*, 1998; *Desorgher et al.*, 1998; *O'Brien et al.*, 2001; *Vassiliadis et al.*, 2002; *Reeves et al.*, 2011] to the solar wind magnetic field [*McPherron et al.*, 2009], and to the solar wind number density [*Lyatsky and Khazanov*, 2008; *Borovsky and Denton*, 2010b; *Balikhin et al.*, 2011]. For the HSS-driven events examined in this study a description of the outer radiation belt in terms of the temperature and density (Figure 7) is found to be useful in explaining changes in the radiation belt. The plots in Figure 5 and Figure 7 make clear that for strong HSSs the higher flux after the flux dropout, compared to the flux prior to dropout (see Figure 5, left plot), is due to an increase in the temperature and the density of the electron distribution over their pre-HSS values (Figure 7, right column, first and second row). For the weak HSSs the lower flux observed after the dropout, compared to the flux prior to dropout (see Figure 5, right plot), is due to the much lower temperature of the electron distribution after the dropout (Figure 7, right column, first row), despite the higher density after the dropout than before the dropout (Figure 7, right column, second row). The before-to-after changes in the flux levels can be explained in a straightforward manner in terms of the evolution of the physical parameters of density and temperature.

5. Conclusions and Summary

[35] The response of various plasma populations in the magnetosphere has been investigated during 93 strong HSSs and during 22 weak HSSs. Analysis has revealed that the magnetospheric system response, as categorized by measurements of different plasmas at geosynchronous orbit, is well correlated with the duration of elevated solar wind velocity (periods of fast solar wind sourced from coronal holes) and with the resulting elevated magnetospheric convection and dayside reconnection rate.

[36] The findings of this study can be summarized as follows:

[37] 1. To understand the response of many of the plasmas within the magnetosphere during HSSs it is necessary to consider the solar wind driver and its time history (e.g., velocity, duration of elevated velocity, presence of a calm) rather than relying on a snapshot of the solar wind parameters or on examination of internal magnetospheric indices alone.

[38] 2. The weak HSSs studied here are on average accompanied by plasmaspheric plumes which have a higher density than those found during strong HSSs. This is largely due to the extended period of low geomagnetic activity for the weak HSSs which allows the plasmasphere to fill to a higher density prior to HSS arrival. This result has implications for potential losses of radiation belt electrons by pitch angle scattering due to EMIC waves within plasmaspheric plumes or for potential losses due to plasmaspheric hiss.

[39] 3. The response of the plasma sheet electron and ion densities and temperatures are correlated with the strength of HSSs. Specifically weak driving produces a weak response. The arrival of HSSs results in a superhot, superdense electron and ion plasma sheet. The duration of this superdense phase depends upon the duration of the compressed high-density solar wind (~1 day for strong HSSs and a few hours for weak HSSs). The duration of the superhot phase depends upon the duration of the fast wind (several days for strong HSSs and ~2 days for weak HSSs) [*Denton and Borovsky*, 2009].

[40] 4. The local-time-averaged multisatellite flux (1.1–1.5 MeV) of electrons in the outer radiation belt before the arrival of weak HSSs (and before the flux dropout) is higher than the local-time-averaged flux level measured after the arrival of weak HSS (and after the flux dropout). The flux (1.1–1.5 MeV) of electrons in the outer radiation belt before the arrival of strong HSSs (and before the flux dropout) is lower than the average flux level measured after the arrival of strong HSSs (and after the flux dropout). A density-temperature description of the outer electron radiation belt indicates that the density recovers from dropout to higher than pre-storm levels during both strong and weak HSSs. However, the lower flux following weak HSSs is due to the fact that the temperature of the radiation belt is much less than its pre-dropout value. For the strong HSSs both the temperature and density are greater after dropout than before dropout. This difference likely reflects a weaker and shorter heating rate for weak HSSs compared to strong HSSs. An obvious difference between the two types of event is the

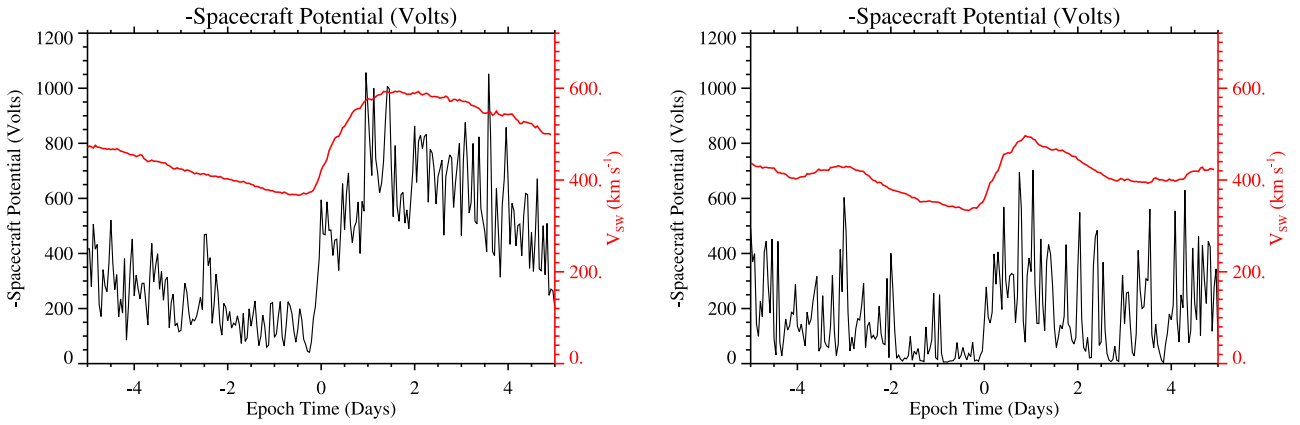

Figure A1. Superposed multisatellite averages of negative spacecraft potential measured around local midnight (22:00–02:00 LT) at geosynchronous orbit for 93 strong HSSs (left column) and 22 weak HSSs (right column) from five days before to five days after zero epoch). The average solar wind velocity for these events is overplotted in red. For the strong HSSs the spacecraft potential remains at highly elevated values for over 4 days. For the weak HSSs the spacecraft potential peaks close to zero epoch and then reduces over the following 1–2 days.

duration and peak velocity of sustained fast solar wind. We speculate that the heating mechanism for the outer electron radiation belt is strongly linked to sustained fast solar wind sourced from coronal holes.

[41] The magnetosphere is a highly coupled system of plasmas overlapping in energy and spatial location. Changes in one area can and do produce changes in other parts of the system and the challenge to theoretical models is to reproduce such coupling in a coherent manner [cf. *Liemohn et al.*, 2006]. Other regions in the magnetosphere not covered in this study are also known to exhibit a response to HSSs include the ionosphere [e.g., *Tsurutani et al.*, 2006b; *Longden et al.*, 2008; *Denton et al.*, 2009; *Pokhotelov et al.*, 2009; *Sojka et al.*, 2009] and the thermosphere/lower atmosphere [e.g., *Clilverd et al.*, 2010; *Rodger et al.*, 2008; *Mlynczak et al.*, 2008, 2010; *Verronen et al.*, 2011]. It would be particularly interesting to examine how the response of these regions during HSSs is dependent on the strength of the driving.

[42] Finally we note the obvious fact that despite the similarity between the events used in this study, and despite the smooth nature of many of the average plots presented in this paper, in reality each CIR and each HSS is different to some degree. No account is made of seasonal trends in the choice of HSSs or the role of the Russell-McPherron effect [*Russell and McPherron*, 1973; *McPherron et al.*, 2009]. One might also ponder whether the structure of the solar wind around the CIR itself [*Borovsky and Denton*, 2010c] and the nature of the shear zone close to the CIR [cf. *Borovsky*, 2006] has any influence on the coupling of the solar wind to the magnetosphere when such solar wind structures impinge on the magnetosphere.

Appendix A: Spacecraft Surface Charging During Strong and Weak Driving

[43] Previous studies have revealed the importance of elevated solar wind speed for spacecraft potential [*DeForest*, 1972; *Hastings and Garrett*, 1996] and specifically during CME-driven and HSS-driven events [*Borovsky et al.*, 1998b; *Denton et al.*, 2006; *Borovsky and Denton*, 2006b]. Here we explore the spacecraft potential on satellites in geosynchronous orbit as a function of HSS strength (speed and duration of fast wind). Figure A1 contains a plot of the (negative) average spacecraft voltage measured by the MPA instrument on LANL satellites around local midnight (22:00–02:00 LT) in geosynchronous orbit as a function of epoch time (*x* axis: 1 h bins) for 93 strong HSSs (right plot) and 22 weak HSSs (left plot) from five days before to five days after zero epoch (for a determination of the derivation of spacecraft charging voltages from the LANL/MPA measurements, see *Thomsen et al.* [1999]).

[44] It is clear that during the calm period prior to both strong HSSs and weak HSSs the spacecraft charging is minimized. Following HSS arrival and the onset of magnetospheric convection (zero epoch), the level of surface charging increases for both strong and weak HSSs. The level of surface charging is significantly greater in magnitude and duration for the strong HSSs than for the weak HSSs. For the strong HSSs the average (negative) charging peaks at ~1000 V and is elevated for >4 days. For the weak HSSs the charging peaks at ~700 V and remains elevated for ~2 days. It is clear by comparison with the solar wind velocity (overplotted in red) that levels of surface charging close to local midnight are elevated whenever the solar wind speed is high and equally whenever the electron plasma sheet temperature remains high (Figure 4) [cf. *Borovsky et al.*, 1998b; *Denton and Borovsky*, 2009].

[45] To investigate this relationship further, we take all available MPA measurements of surface charging between 1989 and 2007 and, after removing magnetosheath intervals, bin these data as a function of local time, and (1) solar wind speed, (2) the *Kp* index, and (3) the *Dst* index. This analysis follows the statistical methodology utilized by *Korth et al.* [1999] and later expanded on by *Denton et al.* [2005, 2006, 2008]. In recent years this methodology has been utilized in several other statistical studies of MPA and SOPA data [e.g., *Borovsky and Denton*, 2006a, 2006b, 2008;

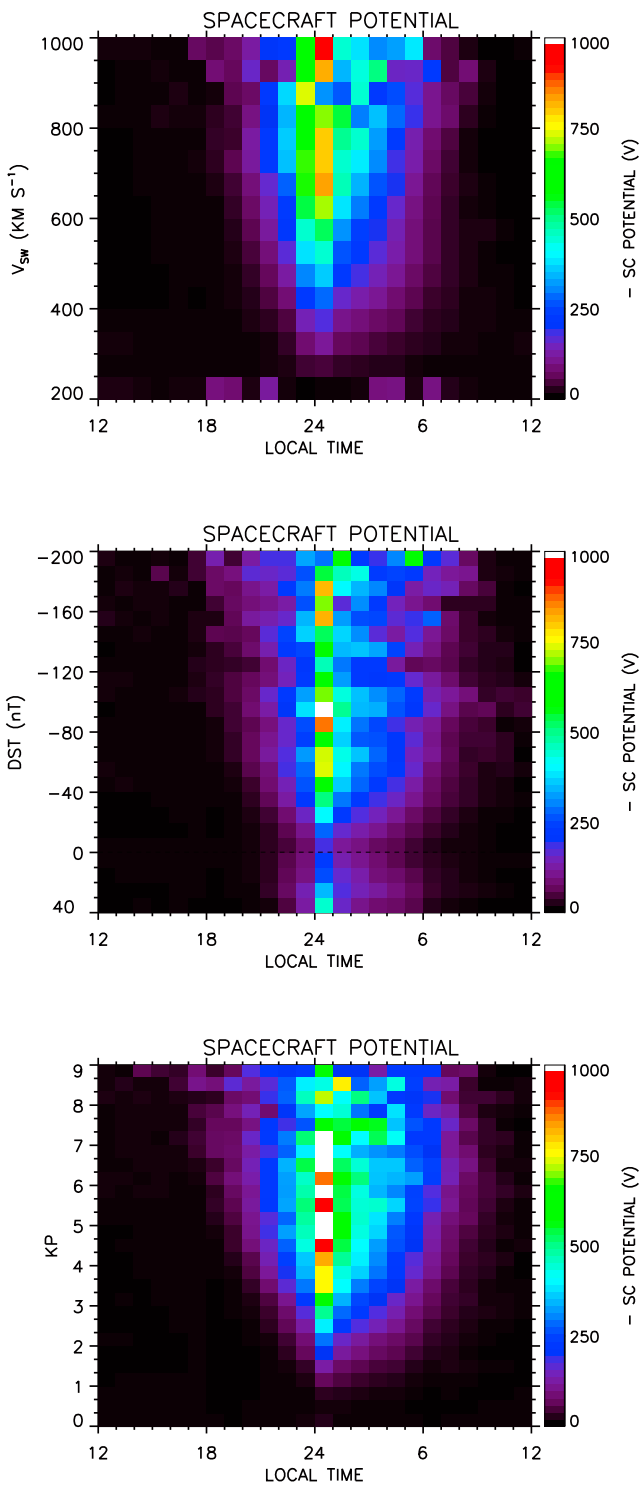

Figure A2. The multisatellite average negative spacecraft potential (1989–2007) at geosynchronous orbit as a function of local time and the solar wind speed (top), the *Dst* index (middle) and the *Kp* index (bottom). In general the negative spacecraft potential increases with increasing solar wind speed (VSW), increasing magnetospheric convection (*Kp* index) and increasing ring current strength (*Dst* index). At the same time the local time region where elevated negative spacecraft potentials occur spreads dawnward and duskward of local midnight.

MacDonald et al., 2008; *Blum et al.*, 2009; *Thomsen et al.*, 2007, 2011]. The methodology utilized here is described in detail by *Denton et al.* [2005].

[46] Figure A2 contains plots of the negative average surface charging as measured by LANL/MPA instruments in geosynchronous orbit as a function of local time (*x* axis: 1 h bins) and (top) the solar wind speed (*y* axis: 16 bins), (middle) the *Dst* index (*y* axis: 24 bins), and (bottom) the *Kp* index (*y* axis: 27 bins). Each plot contains the averages of more than 1 million independent data points. The plots show several interesting features. First it is clear that the average negative spacecraft potential is strongly positively correlated with solar wind speed, the ring current/partial ring current strength (negative *Dst* index), and the strength of magnetospheric convection (*Kp* index). Note in Figure A2 that the superposed average of spacecraft potential can exceed −1000 V for high-speed wind; individual cases can go even higher (to almost −20 kV [M. Thomsen, private communication, 2011]). Also note that the local time region where the surface charging is most extreme is centered on local midnight, where the magnetotail plasma sheet flows into the dipolar magnetosphere and where geosynchronous satellites can enter eclipse.

[47] **Acknowledgments.** We thank Tom Cayton for providing the density and temperature fits to the SOPA data and Michelle Thomsen and Tom Cayton for many useful conversations. We thank Reiner Friedel and Dot Delapp at LANL for providing the SOPA fluxes. We thank Kyoto University for providing the *Dst* values and the U.S. Air Force Research Laboratory, Hanscom Air Force Base, Mass., for providing the Midnight Boundary Index. Research at Lancaster was supported by STFC Grant ST/G002401/1. Work at Los Alamos was supported by the NASA Living with a Star Targeted Research and Technology Program, the NASA CCMSC-24 Program, and the NSF GEM Program. M.H.D. would also like to thank J.E.B. and all in ISR-1 for their generous and frequent hospitality during his visit in summer 2011.

[48] Philippa Browning thanks the reviewers for their assistance in evaluating this paper.

References

Balikhin, M. A., R. J. Boynton, S. N. Walker, J. E. Borovsky, S. A. Billings, and H. L. Wei (2011), Using the NARMAX approach to model the evolution of energetic electron fluxes at geostationary orbit, *Geophys. Res. Lett.*, *38*, L18105, doi:10.1029/2011GL048980.

Bame, S. J., et al. (1993), Magnetospheric plasma analyzer for spacecraft with constrained resources, *Rev. Sci. Instrum.*, *64*, 1026–1033, doi:10.1063/1.1144173.

Bartels, J. (1934), Twenty-seven day recurrences in terrestrial-magnetic and solar activity, 1923–1933, *Terr. Magn. Atmos. Electr.*, *39*(3), 201–202, doi:10.1029/TE039i003p00201.

Belian, R. D., G. R. Gisler, T. Cayton, and R. Christensen (1992), High-Z energetic particles at geostationary orbit during the great proton event series of October 1989, *J. Geophys. Res.*, *97*(A11), 16,897–16,906, doi:10.1029/92JA01139.

Belian, R. D., T. E. Cayton, R. A. Christiansen, J. C. Ingraham, M. M. Meier, G. D. Reeves, and A. J. Lazarus (1996), Relativistic electrons in the outer-zone: An 11 year cycle; Their relation to the solar wind, *AIP Conf. Proc.*, *383*, 13–18, doi:10.1063/1.51526.

Birn, J., M. F. Thomsen, J. E. Borovsky, G. D. Reeves, D. J. McComas, R. D. Belian, and M. Hesse (1998), Substorm electron injections: Geosynchronous observations and test particle simulations, *J. Geophys. Res.*, *103*(A5), 9235–9248, doi:10.1029/97JA02635.

Blum, L. W., E. A. MacDonald, S. P. Gary, M. F. Thomsen, and H. E. Spence (2009), Ion observations from geosynchronous orbit as a proxy for ion cyclotron wave growth during storm times, *J. Geophys. Res.*, *114*, A10214, doi:10.1029/2009JA014396.

Borovsky, J. E. (2006), Eddy viscosity and flow properties of the solar wind: Co-rotating interaction regions, coronal-mass-ejection sheaths, and solar-wind/magnetosphere coupling, *Phys. Plasmas*, *13*, 056505, doi:10.1063/1.2200308.

Borovsky, J. E., and T. E. Cayton (2011), Entropy mapping of the outer electron radiation belt between the magnetotail and geosynchronous orbit, *J. Geophys. Res.*, *116*, A06216, doi:10.1029/2011JA016470.

Borovsky, J. E., and M. H. Denton (2006a), The effect of plasmaspheric drainage plumes on solar-wind/magnetosphere coupling, *Geophys. Res. Lett.*, *33*, L20101, doi:10.1029/2006GL026519.

Borovsky, J. E., and M. H. Denton (2006b), The differences between CME-driven storms and CIR-driven storms, *J. Geophys. Res.*, *111*, A07S08, doi:10.1029/2005JA011447.

Borovsky, J. E., and M. H. Denton (2008), A statistical look at plasmaspheric drainage plumes, *J. Geophys. Res.*, *113*, A09221, doi:10.1029/2007JA012994.

Borovsky, J. E., and M. H. Denton (2009a), Relativistic electron dropouts and recovery: A superposed-epoch study of the magnetosphere and the solar wind, *J. Geophys. Res.*, *114*, A02201, doi:10.1029/2008JA013128.

Borovsky, J. E., and M. H. Denton (2009b), Electron loss rates from the outer electron radiation belt caused by the filling of the outer plasmasphere: The calm before the storm, *J. Geophys. Res.*, *114*, A11203, doi:10.1029/2009JA014063.

Borovsky, J. E., and M. H. Denton (2010a), The magnetic field at geosynchronous orbit during high-speed-stream-driven storms: Connections to the solar wind, the plasma sheet, and the outer electron radiation belt, *J. Geophys. Res.*, *115*, A08217, doi:10.1029/2009JA015116.

Borovsky, J. E., and M. H. Denton (2010b), On the heating of the outer radiation belt to produce high fluxes of relativistic electrons: Measured heating rates at geosynchronous orbit for high-speed-stream-driven storms, *J. Geophys. Res.*, *115*, A12206, doi:10.1029/2010JA015342.

Borovsky, J. E., and M. H. Denton (2010c), Solar wind turbulence and shear: A superposed-epoch analysis of corotating interaction regions at 1 AU, *J. Geophys. Res.*, *115*, A10101, doi:10.1029/2009JA014966.

Borovsky, J. E., and M. H. Denton (2011a), Evolution of the magnetotail energetic-electron population during high-speed-stream-driven storms: Evidence for the leakage of the outer electron radiation belt into the Earth's magnetotail, *J. Geophys. Res.*, *116*, A12228, doi:10.1029/2011JA016713.

Borovsky, J. E., and M. H. Denton (2011b), A survey of the anisotropy of the outer electron radiation belt during high-speed-stream-driven storms, *J. Geophys. Res.*, *116*, A05201, doi:10.1029/2010JA016151.

Borovsky, J. E., and J. T. Steinberg (2006), The "calm before the storm" in CIR/magnetosphere interactions: Occurrence statistics, solar wind statistics, and magnetospheric preconditioning, *J. Geophys. Res.*, *111*, A07S10, doi:10.1029/2005JA011397.

Borovsky, J. E., M. F. Thomsen, and R. C. Elphic (1998a), The driving of the plasma sheet by the solar wind, *J. Geophys. Res.*, *103*(A8), 17,617–17,639, doi:10.1029/97JA02986.

Borovsky, J. E., M. F. Thomsen, D. J. McComas, T. E. Cayton, and D. J. Knipp (1998b), Magnetospheric dynamics and mass flow during the November 1993 storm, *J. Geophys. Res.*, *103*(A11), 26,373–26,394, doi:10.1029/97JA03051.

Carpenter, D. L., B. L. Giles, C. R. Chappell, P. M. E. Decreau, R. R. Anderson, A. M. Persoon, A. J. Smith, Y. Corcuff, and P. Canu (1993), Plasmasphere dynamics in the duskside bulge region: A new look at an old topic, *J. Geophys. Res.*, *98*(A11), 19,243–19,271, doi:10.1029/93JA00922.

Cayton, T. E., and R. D. Belian (2007), Numerical modeling of the synchronous orbit particle analyser (SOPA, Version 2) that flew on S/C 1990–095, *Rep. LA-14335*, Los Alamos Natl. Lab, Los Alamos, N.M.

Cayton, T. E., R. D. Belian, S. P. Gary, T. A. Fritz, and D. N. Baker (1989), Energetic electron components at geosynchronous orbit, *Geophys. Res. Lett.*, *16*(2), 147–150, doi:10.1029/GL016i002p00147.

Chappell, C. R. (1974), Detached plasma regions in the magnetosphere, *J. Geophys. Res.*, *79*(13), 1861–1870, doi:10.1029/JA079i013p01861.

Chappell, C. R., K. K. Harris, and G. W. Sharp (1970), The morphology of the bulge region of the plasmasphere, *J. Geophys. Res.*, *75*(19), 3848–3861, doi:10.1029/JA075i019p03848.

Chen, A. J., and J. M. Grebowsky (1974), Plasma tail interpretations of pronounced detached plasma regions measured by Ogo 5, *J. Geophys. Res.*, *79*(25), 3851–3855, doi:10.1029/JA079i025p03851.

Clilverd, M. A., C. J. Rodger, T. Moffat-Griffin, E. Spanswick, P. Breen, F. W. Menk, R. S. Grew, K. Hayashi, and I. R. Mann (2010), Energetic outer radiation belt electron precipitation during recurrent solar activity, *J. Geophys. Res.*, *115*, A08323, doi:10.1029/2009JA015204.

DeForest, S. E. (1972), Spacecraft charging at synchronous orbit, *J. Geophys. Res.*, *77*(4), 651–659, doi:10.1029/JA077i004p00651.

Denton, M. H., and J. E. Borovsky (2008), Superposed epoch analysis of high-speed-stream effects at geosynchronous orbit: Hot plasma, cold plasma, and the solar wind, *J. Geophys. Res.*, *113*, A07216, doi:10.1029/2007JA012998.

Denton, M. H., and J. E. Borovsky (2009), The superdense plasma sheet in the magnetosphere during high-speed-stream-driven storms: Plasma transport timescales, *J. Atmos. Sol. Terr. Phys.*, *71*, 1045–1058, doi:10.1016/j.jastp.2008.04.023.

Denton, M. H., and T. E. Cayton (2011), Density and temperature of energetic electrons in the Earth's magnetotail derived from high-latitude GPS observations during the declining phase of the solar cycle, *Ann. Geophys.*, *29*, 1755–1763, doi:10.5194/angeo-29-1755-2011.

Denton, M. H., M. F. Thomsen, H. Korth, S. Lynch, J. C. Zhang, and M. W. Liemohn (2005), Bulk plasma properties at geosynchronous orbit, *J. Geophys. Res.*, *110*, A07223, doi:10.1029/2004JA010861.

Denton, M. H., J. E. Borovsky, R. M. Skoug, M. F. Thomsen, B. Lavraud, M. G. Henderson, R. L. McPherron, J. C. Zhang, and M. W. Liemohn (2006), Geomagnetic storms driven by ICME- and CIR-dominated solar wind, *J. Geophys. Res.*, *111*, A07S07, doi:10.1029/2005JA011436.

Denton, M. H., M. F. Thomsen, B. Lavraud, M. G. Henderson, R. M. Skoug, H. O. Funsten, J.-M. Jahn, C. J. Pollock, and J. M. Weygand (2007), Convection-driven transport of plasma sheet material to the inner magnetosphere, *Geophys. Res. Lett.*, *34*, L04105, doi:10.1029/2006GL027886.

Denton, M. H., J. E. Borovsky, R. B. Horne, R. L. McPherron, S. K. Morley, and B. T. Tsurutani (2008), High speed solar wind streams: A call for key research, *Eos Trans. AGU*, *89*(7), 62–63, doi:10.1029/2008EO070002.

Denton, M. H., T. Ulich, and E. Turunen (2009), Modification of midlatitude ionospheric parameters in the F2 layer by persistent high-speed solar wind streams, *Space Weather*, *7*, S04006, doi:10.1029/2008SW000443.

Denton, M. H., J. E. Borovsky, and T. E. Cayton (2010), A density-temperature description of the outer electron radiation belt during geomagnetic storms, *J. Geophys. Res.*, *115*, A01208, doi:10.1029/2009JA014183.

Desorgher, L., P. Buhler, A. Zehnder, E. Daly, and L. Adams (1998), Outer radiation belt variations during 1995, *Adv. Space Res.*, *22*, 83–87, doi:10.1016/S0273-1177(97)01105-8.

Ebihara, Y., and M. Ejiri (2000), Simulation study on fundamental properties of the storm-time ring current, *J. Geophys. Res.*, *105*(A7), 15,843–15,859, doi:10.1029/1999JA900493.

Elphic, R. C., L. A. Weiss, M. F. Thomsen, D. J. McComas, and M. B. Moldwin (1996), Evolution of plasmaspheric ions at geosynchronous orbit during times of high geomagnetic activity, *Geophys. Res. Lett.*, *23*(16), 2189–2192, doi:10.1029/96GL02085.

Elphic, R. C., M. F. Thomsen, J. E. Borovsky, and D. J. McComas (1999), Inner edge of the electron plasma sheet: Empiracal models of boundary location, *J. Geophys. Res.*, *104*(A10), 22,679–22,693, doi:10.1029/1999JA900213.

Fraser, B. J., R. S. Grew, S. K. Morley, J. C. Green, H. J. Singer, T. M. Loto'aniu, and M. F. Thomsen (2010), Storm time observations of electromagnetic ion cyclotron waves at geosynchronous orbit: GOES results, *J. Geophys. Res.*, *115*, A05208, doi:10.1029/2009JA014516.

Freeman, J. W., Jr. (1964), The morphology of the electron distribution in the outer radiation zone and near the magnetospheric boundary as observed by Explorer 12, *J. Geophys. Res.*, *69*(9), 1691–1723, doi:10.1029/JZ069i009p01691.

Fritz, T. A., M. Alothman, J. Bhattacharjya, D. L. Matthews, and J. Chen (2003), Butterfly pitch-angle distributions observed by ISEE-1, *Planet. Space Sci.*, *51*, 205–219, doi:10.1016/S0032-0633(02)00202-7.

Fung, S. F., and L. C. Tan (1998), Time correlation of low-altitude relativistic trapped electron fluxes with solar wind speeds, *Geophys. Res. Lett.*, *25*(13), 2361–2364, doi:10.1029/98GL01717.

Gosling, J. T., J. R. Asbridge, S. J. Bame, and W. C. Feldman (1978), Solar wind stream interfaces, *J. Geophys. Res.*, *83*(A4), 1401–1412, doi:10.1029/JA083iA04p01401.

Gussenhoven, M. S., D. A. Hardy, and N. Heinemann (1983), Systematics of the equatorward diffuse auroral boundary, *J. Geophys. Res.*, *88*(A7), 5692–5708, doi:10.1029/JA088iA07p05692.

Hastings, D., and H. Garrett (1996), *Spacecraft-Environment Interactions*, Cambridge Univ. Press, New York, doi:10.1017/CBO9780511525032.

Hones, E. W., Jr. (1963), Motions of charged particles trapped in the Earth's magnetosphere, *J. Geophys. Res.*, *68*(5), 1209–1219, doi:10.1029/JZ068i005p01209.

Ilie, R., M. W. Liemohn, J. U. Kozyra, and J. E. Borovsky (2010), An investigation of the magnetosphere–ionosphere response to real and idealized co-rotating interaction region events through global magnetohydrodynamic simulations, *Proc. R. Soc. A.*, *466*(2123), 3279–3303, doi:10.1098/rspa.2010.0074.

Jordanova, V. K., Y. S. Miyoshi, S. Zaharia, M. F. Thomsen, G. D. Reeves, D. S. Evans, C. G. Mouikis, and J. F. Fennell (2006), Kinetic simulations of ring current evolution during the Geospace Environment Modeling challenge events, *J. Geophys. Res.*, *111*, A11S10, doi:10.1029/2006JA011644.

Kavanagh, A., and M. H. Denton (2007), High-speed solar wind streams and geospace interactions, *Astron. Geophys.*, *48*, 6.24–6.26, doi:10.1111/j.1468-4004.2007.48624.x.

King, J. H., and N. E. Papitashvili (2005), Solar wind spatial scales in and comparisons of hourly Wind and ACE plasma and magnetic field data, *J. Geophys. Res.*, *110*, A02104, doi:10.1029/2004JA010649.

Korth, H., M. F. Thomsen, J. E. Borovsky, and D. J. McComas (1999), Plasma sheet access to geosynchronous orbit, *J. Geophys. Res.*, *104*(A11), 25,047–25,061, doi:10.1029/1999JA900292.

Kovalevskiy, I. V. (1980), Ion-cyclotron instability in the frontal boundary layer of the geomagnetosphere produced by detached plasma clouds, *Geomagn. Aeron.*, *20*, 338–345.

Kovalevskiy, I. V. (1981), Cyclotron instability during interaction of detached plasma regions with the plasma sheet during substorms, *Geomagn. Aeron.*, *21*, 83–86.

Kozyra, J. U., and M. W. Liemohn (2003), Ring current energy input and decay, *Space Sci. Rev.*, *109*, 105–131, doi:10.1023/B:SPAC.0000007516.10433.ad.

Lam, M. M., R. B. Horne, N. P. Meredith, and S. A. Glauert (2007), Modeling the effects of radial diffusion and plasmaspheric hiss on outer radiation belt electrons, *Geophys. Res. Lett.*, *34*, L20112, doi:10.1029/2007GL031598.

Lavraud, B., M. H. Denton, M. F. Thomsen, J. E. Borovsky, and R. H. W. Friedel (2005), Superposed epoch analysis of cold dense plasma access to geosynchronous orbit, *Ann. Geophys.*, *23*, 2519–2529, doi:10.5194/angeo-23-2519-2005.

Lavraud, B., M. F. Thomsen, S. Wing, M. Fujimoto, M. H. Denton, J. E. Borovsky, A. Åsnes, K. Seki, and J. M. Weygand (2006), Observation of two distinct cold, dense ion populations at geosynchronous orbit: Local time asymmetry, solar wind dependence and origin, *Ann. Geophys.*, *24*, 3451–3465, doi:10.5194/angeo-24-3451-2006.

Lawrence, D. J., M. F. Thomsen, J. E. Borovsky, and D. J. McComas (1999), Measurements of early and late-time plasmasphere refilling as observed from geosynchronous orbit, *J. Geophys. Res.*, *104*(A7), 14,691–14,704, doi:10.1029/1998JA900087.

Lemon, C. L., and T. P. O'Brien (2008), A solar wind model of geosynchronous plasma moments, *Adv. Space Res.*, *41*, 1226–1233, doi:10.1016/j.asr.2007.08.028.

Lezniak, T. W., R. L. Arnoldy, G. K. Parks, and J. R. Winkler (1968), Measurements and intensity of energetic electrons at the equator at 6.6 R_E, *Radio Sci.*, *3*, 710–714.

Liemohn, M. W., and A. A. Chan (2007), Unraveling the causes of radiation belt enhancements, *Eos Trans. AGU*, *88*(42), 425, doi:10.1029/2007EO420001.

Liemohn, M. W., J. U. Kozyra, M. F. Thomsen, J. L. Roeder, G. Lu, J. E. Borovsky, and T. E. Cayton (2001), Dominant role of the asymmetric ring current in producing stormtime *Dst**, *J. Geophys. Res.*, *106*(A6), 10,883–10,904, doi:10.1029/2000JA000326.

Liemohn, M. W., A. J. Ridley, J. U. Kozyra, D. L. Gallagher, M. F. Thomsen, M. G. Henderson, M. H. Denton, P. C. Brandt, and J. Goldstein (2006), Analyzing electric field morphology through data-model comparisons of the GEM IM/S assessment challenge events, *J. Geophys. Res.*, *111*, A11S11, doi:10.1029/2006JA011700.

Longden, N., M. H. Denton, and F. Honary (2008), Particle precipitation during ICME-driven and CIR-driven geomagnetic storms, *J. Geophys. Res.*, *113*, A06205, doi:10.1029/2007JA012752.

Lyatsky, W., and G. V. Khazanov (2008), Effect of solar wind density on relativistic electrons at geosynchronous orbit, *Geophys. Res. Lett.*, *35*, L03109, doi:10.1029/2007GL032524.

Lyons, L. R., R. M. Thorne, and C. F. Kennel (1972), Pitch-anlge diffusion of radiation belt electrons within the plasmasphere, *J. Geophys. Res.*, *77*(19), 3455–3474, doi:10.1029/JA077i019p03455.

MacDonald, E. A., M. H. Denton, M. F. Thomsen, and S. P. Gary (2008), Superposed epoch analysis of a whistler instability criterion at geosynchronous orbit during geomagnetic storms, *J. Atmos. Sol. Terr. Phys.*, *70*, 1789–1796, doi:10.1016/j.jastp.2008.03.021.

McComas, D. J., S. J. Bame, B. L. Barraclough, J. R. Donart, R. C. Elphic, J. T. Gosling, M. B. Moldwin, K. R. Moore, and M. F. Thomsen (1993), Magnetospheric Plasma Analyzer: Initial three-spacecraft observations from geosynchronous orbit, *J. Geophys. Res.*, *98*(A8), 13,453–13,465, doi:10.1029/93JA00726.

McPherron, R. L., and J. Weygand (2006), The solar wind and geomagnetic activity as a function of time relative to corotating interaction regions, in *Recurrent Magnetic Storms: Corotating Solar Wind Streams*, *Geophys. Monogr. Ser.*, vol. 167, edited by B. Tsurutani et al., pp. 125–137, AGU, Washington, D. C., doi:10.1029/167GM12.

McPherron, R. L., D. N. Baker, and N. U. Crooker (2009), Role of the Russell-McPherron effect in the acceleration of relativistic electrons, *J. Atmos. Sol. Terr. Phys.*, *71*, 1032–1044, doi:10.1016/j.jastp.2008.11.002.

Meredith, N. P., R. B. Horne, S. A. Glaurt, R. M. Thorne, D. Summers, J. M. Albert, and R. R. Anderson (2006), Energetic outer zone electron loss timescales during low geomagnetic activity, *J. Geophys. Res.*, *111*, A05212, doi:10.1029/2005JA011516.

Mlynczak, M. G., F. J. Martin-Torres, C. J. Mertens, B. T. Marshall, R. E. Thompson, J. U. Kozyra, E. E. Remsberg, L. L. Gordley, J. M. Russell III, and T. Woods (2008), Solar-terrestrial coupling evidenced by periodic behavior in geomagnetic indexes and the infrared energy budget of the thermosphere, *Geophys. Res. Lett.*, *35*, L05808, doi:10.1029/2007GL032620.

Mlynczak, M. G., L. A. Hunt, J. U. Kozyra, and J. M. Russell (2010), Short-term periodic features observed in the infrared cooling of the thermosphere and in solar and geomagnetic indexes from 2002 to 2009, *Proc. R. Soc. A*, *466*, 3409–3419, doi:10.1098/rspa.2010.0077.

Morley, S. K., R. H. W. Friedel, E. L. Spanswick, G. D. Reeves, J. T. Steinberg, J. Koller, T. Cayton, and E. Noveroske (2010), Dropouts of the outer electron radiation belt in response to solar wind stream interfaces: Global positioning system observations, *Proc. R. Soc. A*, *466*, 3329–3350, doi:10.1098/rspa.2010.0078.

Nagai, T. (1988), "Space weather forecast" prediction of relativistic electron intensity at synchronous orbit, *Geophys. Res. Lett.*, *15*(5), 425–428, doi:10.1029/GL015i005p00425.

O'Brien, T. P., R. L. McPherron, D. Sornette, G. D. Reeves, R. Friedel, and H. J. Singer (2001), Which magnetic storms produce relativistic electrons at geosynchronous orbit?, *J. Geophys. Res.*, *106*(A8), 15,533–15,544, doi:10.1029/2001JA000052.

Onsager, T. G., G. Rostoker, H.-J. Kim, G. D. Reeves, T. Obara, H. J. Singer, and C. Smithtro (2002), Radiation belt electron flux dropouts: Local time, radial, and particle-energy dependence, *J. Geophys. Res.*, *107*(A11), 1382, doi:10.1029/2001JA000187.

Paulikas, G. A., and J. B. Blake (1979), Effects of the solar wind on magnetospheric dynamics: Energetic electrons at the synchronous orbit, in *Quantitative Modeling of Magnetospheric Processes*, *Geophys. Monogr. Ser.*, vol. 21, edited by W. P. Olsen, pp. 180–202, AGU, Washington, D.C., doi:10.1029/GM021p0180.

Pfitzer, K. A., T. W. Lezniak, and J. R. Winckler (1969), Experimental verification of drift-shell splitting in the distorted magnetosphere, *J. Geophys. Res.*, *74*(19), 4687–4693, doi:10.1029/JA074i019p04687.

Pierrard, V., and J. Lemaire (1996), Fitting the AE-8 energy spectra with two Maxwellian functions, *Radiat. Meas.*, *26*, 333–337, doi:10.1016/1350-4487(96)00057-1.

Pokhotelov, D., C. N. Mitchell, P. T. Jayachandran, J. W. MacDougall, and M. H. Denton (2009), Ionospheric response to the CIR-driven geomagnetic storm of October 2002, *J. Geophys. Res.*, *114*, A12311, doi:10.1029/2009JA014216.

Reeves, G. D., K. L. McAdams, R. H. W. Friedel, and T. P. O'Brien (2003), Acceleration and loss of relativistic electrons during geomagnetic storms, *Geophys. Res. Lett.*, *30*(10), 1529, doi:10.1029/2002GL016513.

Reeves, G. D., S. K. Morley, R. H. W. Friedel, M. G. Henderson, T. E. Cayton, G. Cunningham, J. B. Blake, R. A. Christensen, and D. Thomsen (2011), On the relationship between relativistic electron flux and solar wind velocity, Paulikas and Blake revisited, *J. Geophys. Res.*, *116*, A02213, doi:10.1029/2010JA015735.

Rodger, C. J., T. Raita, M. A. Clilverd, A. Seppälä, S. Dietrich, N. R. Thomsen, and T. Ulich (2008), Observations of relativistic electron precipitation from the radiation belts driven by EMIC waves, *Geophys. Res. Lett.*, *35*, L16106, doi:10.1029/2008GL034804.

Russell, C. T., and R. L. McPherron (1973), Semiannual variation of geomagnetic activity, *J. Geophys. Res.*, *78*(1), 92–108, doi:10.1029/JA078i001p00092.

Selesnick, R. S., and J. B. Blake (2002), Relativistic electron drift shell splitting, *J. Geophys. Res.*, *107*(A9), 1265, doi:10.1029/2001JA009179.

Sojka, J. J., and G. L. Wrenn (1985), Refilling of geosynchronous flux tubes as observed at the equator by GEOS 2, *J. Geophys. Res.*, *90*(A7), 6379–6385, doi:10.1029/JA090iA07p06379.

Sojka, J. J., R. L. McPherron, A. P. van Eyken, M. J. Nicolls, C. J. Heinselman, and J. D. Kelly (2009), Observations of ionospheric heating during the passage of solar coronal hole fast streams, *Geophys. Res. Lett.*, *36*, L19105, doi:10.1029/2009GL039064.

Spiro, R. W., M. Harel, R. A. Wolf, and P. H. Reiff (1981), Quantitative simulation of a magnetospheric substorm 3. Plasmaspheric electric fields and evolution of the plasmapause, *J. Geophys. Res.*, *86*(A4), 2261–2272, doi:10.1029/JA086iA04p02261.

Su, Y.-J., M. F. Thomsen, J. E. Borovsky, and D. J. Lawrence (2001), A comprehensive survey of plasmasphere refilling at geosynchronous orbit, *J. Geophys. Res.*, *106*(A11), 25,615–25,629, doi:10.1029/2000JA000441.

Summers, D., B. Ni, and N. P. Meredith (2007), Timescales for radiation belt electron acceleration and loss due to resonant wave-particle interactions: 2. Evaluation for VLF chorus, ELF hiss, and electromagnetic

ion cyclotron waves, *J. Geophys. Res.*, *112*, A04207, doi:10.1029/2006JA011993.

Thomsen, M. F. (2004), Why *Kp* is such a good measure of magnetospheric convection, *Space Weather*, *2*, S11004, doi:10.1029/2004SW000089.

Thomsen, M. F., E. Noveroske, J. E. Borovsky, and D. J. McComas (1999), Calculation of moments from measurements by the Los Alamos Magnetospheric Plasma Analyzer, *Rep. LA-13566-MS*, Los Alamos Natl. Lab, Los Alamos, N. M., doi:10.2172/8188.

Thomsen, M. F., J. E. Borovsky, R. M. Skoug, and C. W. Smith (2003), Delivery of cold, dense plasma sheet material into the near-Earth region, *J. Geophys. Res.*, *108*(A4), 1151, doi:10.1029/2002JA009544.

Thomsen, M. F., M. H. Denton, B. Lavraud, and M. Bodeau (2007), Statistics of plasma fluxes at geosynchronous orbit over more than a full solar cycle, *Space Weather*, *5*, S03004, doi:10.1029/2006SW000257.

Thomsen, M. F., M. H. Denton, V. K. Jordanova, L. Chen, and R. M. Thorne (2011), Free energy to drive the magnetosonic instability at geosynchronous orbit, *J. Geophys. Res.*, *116*, A08220, doi:10.1029/2011JA016644.

Thorne, R. M., R. B. Horne, V. K. Jordanova, J. Bortnik, and S. Glauert (2006), Interaction of EMIC waves with thermal plasma and radiation belt particles, in *Magnetospheric ULF Waves*, *Geophys. Monogr. Ser.*, vol. 169, edited by K. Takahashi et al., 213–223, AGU, Washington, D. C., doi:10.1029/169GM14.

Troshichev, O. A., V. G. Andrezen, S. Vennerstrøm, and E. Friis-Christensen (1988), Magnetic activity in the polar cap: A new index, *Planet. Space Sci.*, *36*, 1095–1102, doi:10.1016/0032-0633(88)90063-3.

Tsurutani, B. T., W. D. Gonzalez, A. L. C. Gonzalez, F. Tang, J. K. Arballo, and M. Okada (1995), Interplanetary Origin of Geomagnetic Activity in the Declining Phase of the Solar Cycle, *J. Geophys. Res.*, *100*(A11), 21,717–21,733, doi:10.1029/95JA01476.

Tsurutani, B. T., et al. (2006a), Corotating solar wind streams and recurrent geomagnetic activity: A review, *J. Geophys. Res.*, *111*, A07S01, doi:10.1029/2005JA011273.

Tsurutani, B. T., A. J. Mannucci, B. A. Iijima, A. Kamjathy, A. Saito, T. Tsuda, O. P. Verkhoglyadova, W. D. Gonzalez, and F. L. Guamieri (2006b), Dayside ionospheric (GPS) response to corotating solar wind streams, in *Recurrent Magnetic Storms: Corotating Solar Wind Streams*, *Geophys. Monogr. Ser.*, vol. 167, edited by B. Tsurutani et al., pp. 245–270, AGU, Washington, D. C., doi:10.1029/167GM20.

Vassiliadis, D., A. J. Klimas, S. G. Kanekal, D. N. Baker, and R. S. Weigel (2002), Long-term-average, solar cycle, and seasonal response of magnetospheric energetic electrons to the solar wind speed, *J. Geophys. Res.*, *107*(A11), 1383, doi:10.1029/2001JA000506.

Verronen, P. T., C. J. Rodger, M. A. Clilverd, and S. Wang (2011), First evidence of mesospheric hydroxyl response to electron precipitation from the radiation belts, *J. Geophys. Res.*, *116*, D07307, doi:10.1029/2010JD014965.

M. H. Denton, Department of Physics, Lancaster University, Lancaster, LA1 4YB Lancashire, UK. (m.denton@lancaster.ac.uk)

J. E. Borovsky, Space Science and Applications (ISR-1), Los Alamos National Laboratory, Mail Stop D466, Los Alamos, NM 87545, USA.